1-1-2008

The frictional response of patterned soft polymer surfaces.

Charles J. Rand
University of Massachusetts Amherst

THE FRICTIONAL RESPONSE OF PATTERNED SOFT POLYMER SURFACES

A Dissertation Presented

by

CHARLES J. RAND

Submitted to the Graduate School of the University of Massachusetts in partial fulfillment of the requirements for the degree of

DOCTOR OF PHILOSOPHY

September, 2008

Polymer Science and Engineering

THE FRICTIONAL RESPONSE OF PATTERNED SOFT POLYMER SURFACES

A Dissertation Presented

By

CHARLES J. RAND

Approved as to style and content by:

_____

Alfred J. Crosby, Chair

_____

Kenneth R. Carter, Member

_____

Jonathan P. Rothstein, Member

_____

Shaw Ling Hsu, Department Head
Polymer Science & Engineering

THE FRICTIONAL RESPONSE OF PATTERNED SOFT POLYMER SURFACES

A Dissertation Presented

By

CHARLES J. RAND

Approved as to style and content by:

Alfred J. Crosby, Chair

Kenneth R. Carter, Member

Jonathan P. Rothstein, Member

Shaw Ling Hsu, Department Head
Polymer Science & Engineering

DEDICATION

To my parents.

ACKNOWLEDGEMENTS

First and foremost, I would like to thank my advisor Alfred J. Crosby. Al was a new professor when I joined his group and this allowed me the opportunity to help build a lab and see first hand all that was required in developing a successful research group. His excitement for science kept me motivated and on track, even during despairing times in the laboratory. I have never met a person so excited about science and most likely never will. It was impossible to avoid having this excitement rub off on any of the group members and this was noticeable in all of the work coming out of the group. I consider joining the Crosby group as one of the best decisions of my life and after 5 years I have gained more from this experience than any other of my educational experiences. Al was so much more than just an advisor; I also consider him and his wife Kerry as good friends, always willing to help, even outside of the department and research. I can not write enough to thank the two of them.

I would also like to thank my thesis committee members Prof. Ken R. Carter and Prof. Jonathan P. Rothstein. They devoted time in their busy schedules to serve on my committee and provided insight from their respective expertise. Their advice and comments helped me get the most out of this experience.

I would like to thank all of my friends in Ohio (Doug, Mireille, Chris, Aaron, Joe A., Joe S., Judy, Mo, and others). It was trips home that help me keep my sanity. I would especially like to thank Hossein, Ruthie, and Bella who are more than friends, but family to me.

I would like to thank my group mates (Edwin Chan, Jong-Young Lee, Mark Hageman, Doug Holmes, Jessica Zimberlin, Derek Breid, Chelsea Davis, Sam

Pendergraph, Jun Cui, Hyun-Suk Kim, Yuri Ebata, Guillaume Miquelard, Santanu Kundu, and Kyriaki Kalaitzidou) and other students that I have worked with while at UMass. I would especially like to thank Edwin and Jong-Young who started around the same time as I did and can remember when the Crosby group could fit into one car not the bus he would need these days. I will miss arguing with Jong-Young about why he shouldn't be a Boston sports fan and also teaching him everything he needed to know about the USA that he couldn't read in a book or learn from TV. I will also miss his stories of Taiwan and growing up and especially the daily "what is ..." question he would ask about random topics. Edwin was a lab-mate, officemate, and also a roommate for a year. The fact that we still talk is a testament of our friendship, usually people grow to despise someone they see that much. Thanks also to Chelsea and Doug for putting up with me in the office. Also to Doug for keeping me up to date with tap list at the Dove and was always willing to talk sports.

I also want to thank Greg Su, Renee Sweeney, Mary Morrissey, and Lauren Hazel, who all had the opportunity to conduct research with me. I would like to thank all of the past and present faculty and staff of the PSE department who helped along the way

Last, but certainly not least, I want to thank my Family. To my brothers, Doug and Bill, I have enjoyed meeting once a year at the NCAA hockey tournament and all of the fun we have had exploring each city the tournament has been held in. I also enjoyed visiting Chicago once a year and hanging out as a Rand of Brothers. To my parents, Julie and George, I dedicate this thesis to you. With out your support and encouragement this would have never happened. Words can not express the thanks that I owe you.

ABSTRACT

THE FRICTIONAL RESPONSE OF PATTERNED SOFT POLYMER SURFACES

DECEMBER 2008

CHARLES J. RAND, B.S., THE UNIVERSITY OF AKRON

M.S., UNIVERSITY OF MASSACHUSETTS AMHERST

PH.D., UNIVERSITY OF MASSACHUSETTS AMHERST

Directed by: Professor Alfred J. Crosby

Friction plays an intricate role in our everyday lives, it is therefore critical to understand the underlying features of friction to better help control and manipulate the response anywhere two surfaces in contact move past each other by a sliding motion. Here we present results targeting a thorough understanding of soft material friction and how it can be manipulated with patterns. We found that the naturally occurring length scale or periodicity (λ) of frictionally induced patterns, Schallamach waves, could be described using two materials properties (critical energy release rate ($\mathcal{G}_c$) and complex modulus (E*), i.e. $\lambda \propto \mathcal{G}_c/E^*$). Following this, we evaluated the effect of a single defect at a sliding interface. Sliding over a defect can be used to model the sliding from one feature to another in a patterned surface. Defects decreased the sliding frictional force by as much as 80% sliding and this decrease was attributed to changes in tangential stiffness of the sliding interface. The frictional response of surface wrinkles, where multiple edges or defects are acting in concert, was also evaluated. Wrinkles were shown to decrease friction (F) and changes in contact area (A) could not describe this decrease. A tangential stiffness correction factor (f_x) and changes in the critical energy release rate were used to

describe this deviation ($F \propto \mathcal{G}_c * A * f_x / \ell$, where ℓ is a materials defined length scale of dissipation). This scaling can be used to describe the friction of any topographically patterned surface including the Gecko's foot, where the feature size is smaller than ℓ and thus replaces ℓ, increasing the friction compared to a flat surface. Also, mechanically-induced surface defects were used to align osmotically driven surface wrinkles by creating stress discontinuities that convert the global biaxial stress state to local uniaxial stresses. Defect spacing was used to control the alignment process at the surface of the wrinkled rigid film/soft elastomer interface. These aligned wrinkled surfaces can be used to tune the adhesion and friction of an interface. The work presented here gives insight into tuning the friction of a soft polymeric surface as well as understanding the friction of complex hierarchical structures.

CONTENTS

LIST OF TABLES

Table Page

LIST OF FIGURES

CHAPTER 1

INTRODUCTION

1.1 Project Overview

Friction plays an intricate role in our everyday lives everything from the tires on our cars to hard drives in our computers. It is therefore critical to understand the underlying features of friction to better help control and manipulate the response anywhere two surfaces in contact move past each other by a sliding motion. While the topic of friction is an overwhelming and broad subject, the focus of this research was soft elastomeric friction. Specifically, we were interested in the effect of interfacial topographical patterns on the frictional response. Our goal was to not only develop guiding principles for the design of pattern structures for enhanced response, but also to use the pattern response to provide insight into the fundamental mechanisms of solid friction.

In 1699, Amontons rediscovered the original results described by Leonardo da Vinci, force is proportional to applied load ($F = \mu * P$). This relationship was received with criticism until it was verified by Coulomb in 1781. Since then friction has been described largely in terms of a coefficient of friction, which is often regarded as a material property, but seems to combine material properties and other variables including testing geometry. One problem with Amontons law is that it does not properly describe soft material friction or friction at low normal loads. In soft material friction, sliding with contact can proceed under no applied normal load and even under negative loads, in both case Amontons law fails to hold. Bowden and Tabor presented the adhesional theory of friction, in which they stated that frictional force (F) was equal to the product of the true

contact area (A) and the interfacial shear strength (τ)[1]. Interfacial shear strength, often referred to as a material property, assumes that thickness effects, edge effects, and other geometric considerations do not greatly change the sliding force. The scaling thus describes the sliding of thick, smooth soft material very accurately, but fails to accurately predict the frictional force of soft topologically patterned surface. Understanding the frictional force of patterned surfaces is critical to their use in real world applications and hence this scaling needs to be adapted to account for these surfaces.

Recent research in adhesion has focused on understanding and mimicking the hierarchical structure of the gecko's foot to enhance adhesion [2-4]. The gecko's foot is composed of hair like features (seta) with finer structure located on the tips (spatula). This hierarchical arrangement plays a critical role in the gecko's ability to climb walls. Inspired by this control, synthetic gecko structures and patterns in general have been shown to have enhanced control of adhesion [5-11]. This enhancement has been linked to several mechanisms, which relate pattern length scales to length scales defined by the materials. Although this understanding of patterned control of interfacial properties has been developed for normal adhesion, mode I separation, the impact of interfacial patterns on shear properties such as friction has not been explored in great detail. Therefore, we focused on the use of topographically patterned surfaces to better understand the relationship between bulk and interfacial materials properties and pattern parameters in the control of soft material friction.

Accordingly, we conducted research targeting a thorough understanding soft material friction and how it can be manipulated with patterns. This thesis is divided into four parts: 1) understanding the length scale of naturally occurring surface features during

sliding; 2) evaluating the effect of a single surface feature on sliding forces; 3) the frictional response of multiple low aspect ratio surfaces features; and 4) a new robust method for making anisotropic surface features. First, we evaluated naturally occurring patterns, Schallamach waves, which occur in soft material friction. Schallamach waves are frictionally induced elastic instabilities that provide displacement between a rigid material and a soft surface. In chapters 2 and 3 we present background to Schallamach waves and discuss the mechanism of sliding friction. In Chapter 3 we use materials properties to describe the length scales associated with these naturally occurring surface features, Schallamach waves. In chapters 4 and 5, we discuss two projects that developed our understanding of how patterns influence Schallamach waves and soft material sliding, in general. In chapter 4, we understand the effect of a single defect. Patterns can be described as a periodic arrangement of edges, or boundaries. In nature, these edges are often physical, or topographical. Before understanding the effect of multiple edges on a sliding contact, it was critical to quantify the impact of a single physical edge on sliding friction for a soft interface. Building on the effects of a single topographic feature in Chapter 5, we discuss the characterization of topographical patterns, where multiple edges are acting in concert. The surface patterns that we used were based on surface wrinkling, and we show how these surface features can be used to tune sliding friction. In Chapter 6, we introduce a simple process for creating materials that produce osmotically-driven surface wrinkles with long-range alignment, sans lithographically defined topography and selective oxidation. Mechanically-induced surface defects create stress discontinuities that convert the global biaxial stress state to local uniaxial stresses, producing aligned wrinkles across the surface. We discuss the critical variables to control

the alignment of surface wrinkles using imposed interfacial defects and discuss how the work presented in Chapters 4 and 5 can be used to understand the sliding frictional response of these anisotropic surfaces. All of the research presented in this thesis lays the fundamental groundwork for understanding the frictional response of hierarchical structures both synthetic and in nature.

CHAPTER 2

SCHALLAMACH WAVES

2.1 FRICTIONAL MECHANISMS

Contacting solid surfaces may slide past each other by one of three possible displacement mechanisms true sliding, stick-slip, or Schallamach waves. A schematic of the data associated with all three frictional responses is shown in figure 2.1. True sliding proceeds by exceeding a critical initiation force (static coefficient of friction). Sliding then continues at a constant kinetic force (kinetic coefficient of friction). Stick-slip, as described by Bowden and Tabor, does not proceed by continuous sliding, but rather "a series of intermittent jerks"[1]. In the case of stick slip, the slider moves after overcoming the static resistance to motion. During movement, the lateral force drops until motion is suspended due to interfacial pinning. The force again reaches the critical force, and the cycle repeats (figure 2.1). Stick slip is prevalent in many soft materials. The third possible displacement mechanism is Schallamach waves. In 1971, Schallamach imaged the contact area between rubber and a rigid surface. This imaging allowed him to see that the motion between the two surfaces was predominately created by "waves of detachment" and not true sliding [12]. This phenomenon has since become known as Schallamach waves. One should note that from the evaluation of data alone, stick-slip can be confused with Schallamach waves and imaging the contact area is currently the only way to differentiate the two mechanisms.

2.2 SCHALLAMACH WAVES

Schallamach waves most commonly form when the interface created by an elastomeric material is sheared. Described here will be the case of a rigid hemispherical

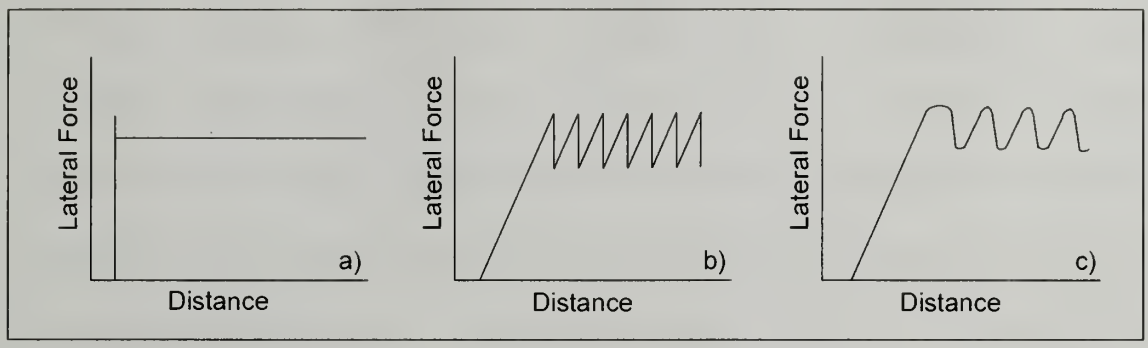

Figure 2.1: Schematics of data for (a) true-sliding, (b) stick-slip, and (c) Schallamach waves.

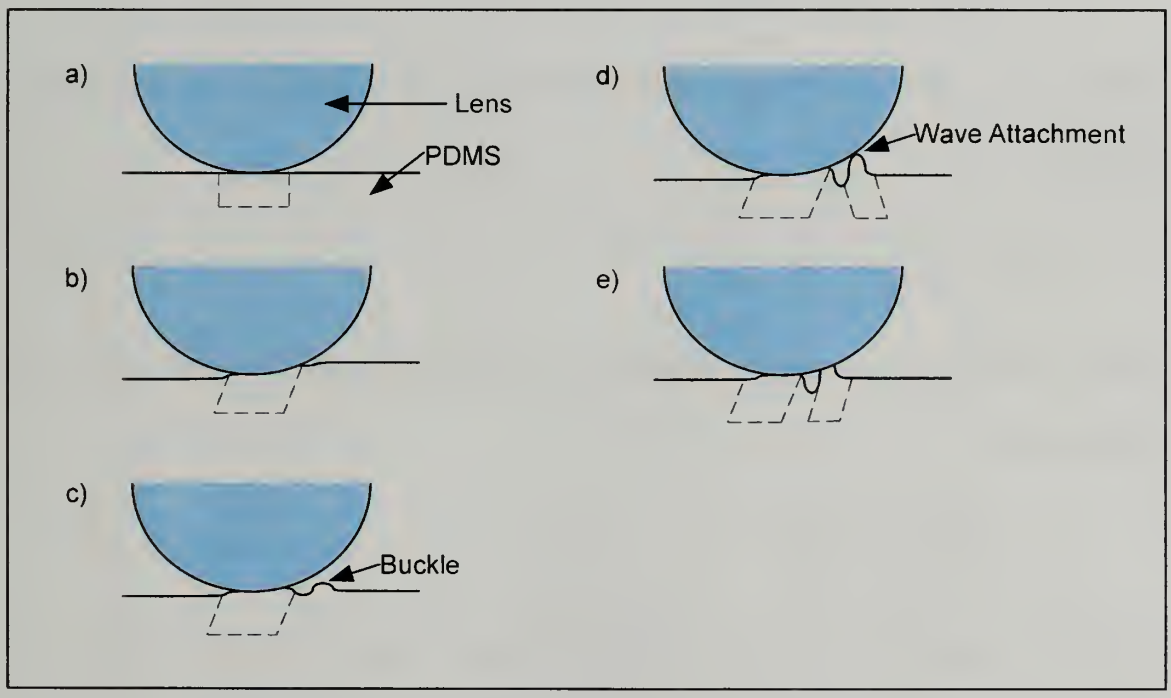

Figure 2.2: Schematic of the formation, attachment, and propagation of Schallamach waves.

slider sheared along a soft adhesive elastomeric film, but the process is general and can relate to the inverse case where a soft slider moves along a rigid surface (figure 2.2). Upon being brought into contact, the two materials form an initial contact area, $A=\pi a^2$, that is determined by the normal load applied (P), contact geometry, elastic modulus of the two materials (E*), and the interfacial adhesion, $\mathcal{G}_c$. The relationship between these parameters is described by the theory of Johnson, Kendall, and Roberts[13]:

$$a^3 = \frac{3R}{4E^*}\left(P + 3\pi\mathcal{G}R + \left(6\pi\mathcal{G}RP + (3\pi\mathcal{G}R)^2\right)^{1/2}\right), \qquad 2.1$$

where R is the radius of curvature, defined by the radius of curvature of the two surfaces in contact:

$$\frac{1}{R} = \frac{1}{R_1} + \frac{1}{R_2} \qquad 2.2$$

and E* is the effective modulus defined by the modulus (E) and Poisson's ratio (ν) of each surface:

$$\frac{1}{E^*} = \frac{\left(1-\nu_1^2\right)}{E_1} + \frac{\left(1-\nu_2^2\right)}{E_2}. \qquad 2.3$$

The initial contact area is shown in the first image of figure 2.3. Upon shearing the interface, a compressive zone develops ahead of the slider and a tensile zone in the rear, which is shown in figure 2.2(b). For soft materials, the contact area becomes asymmetrical during shearing, due to a peeling of the trailing edge in the tensile region and more subtle peeling from the front edge. If the energy stored during shear becomes greater than the adhesive energy holding the interface together, the interface will fail as a whole and true sliding will occur. With strong adhesive forces, the compressive forces ahead of the contact can reach a critical point where the material ahead of the slider will

buckle as shown in figure 2.2(c). Assuming the interface holds, the buckle will eventually attach on the slider incorporating the buckle into the contact area, which is shown in figure 2.2(d). This buckle addition leads to incorporation of a "pocket" of air, which is open to the environment along the edge parallel to the direction of travel. Once the buckle attaches to the slider, the wave passes through the contact area if there is a balance between the energy required to sustain the buckle and the adhesive forces (figure 2.2(e)). If the adhesive energy on either side of the wave is less than the energy needed to sustain the buckle, slip will occur and the wave will collapse. Before attachment of the buckle, if the adhesive energy is overcome by the energy required to buckle or compress the buckle, the contact area will slip. This slip is marked by an attachment in the trailing edge. Stick-slip can happen if a buckle does not form, while the material is buckling, or while the buckle is attaching.

A typical force curve for the onset and propagation of Schallamach waves is illustrated in figure 2.3. The initial shearing of the interface is dictated by the shear modulus of the material. As noted above, the interface is sheared until a critical stress is reached at the interface and a buckle forms as seen in the second image of figure 2.3. The force required to buckle is roughly the average lateral force of the steady state process.

Schallamach wave formation is essentially a surface buckling phenomenon. Surface buckling was initially analyzed by Green and Zerna, in their theoretical work on the indention of an elastomeric surface[14], which was then extended to anisotropic networks by Biot[15]. The buckling that occurs during Schallamach wave formation is similar to wrinkles induced by applying strain to a confined soft elastomeric substrate [16-25]. Schallamach waves are single wrinkles that form at a surface due the

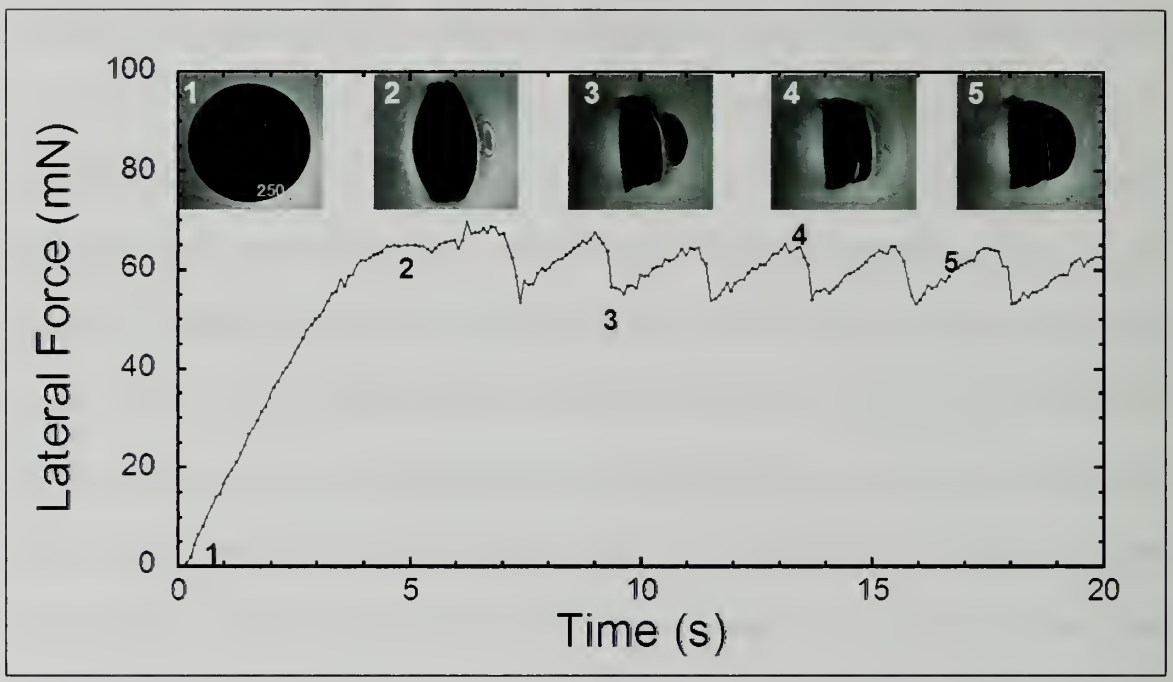

Figure 2.3: Typical lateral force versus time curve for samples with Schallamach waves.

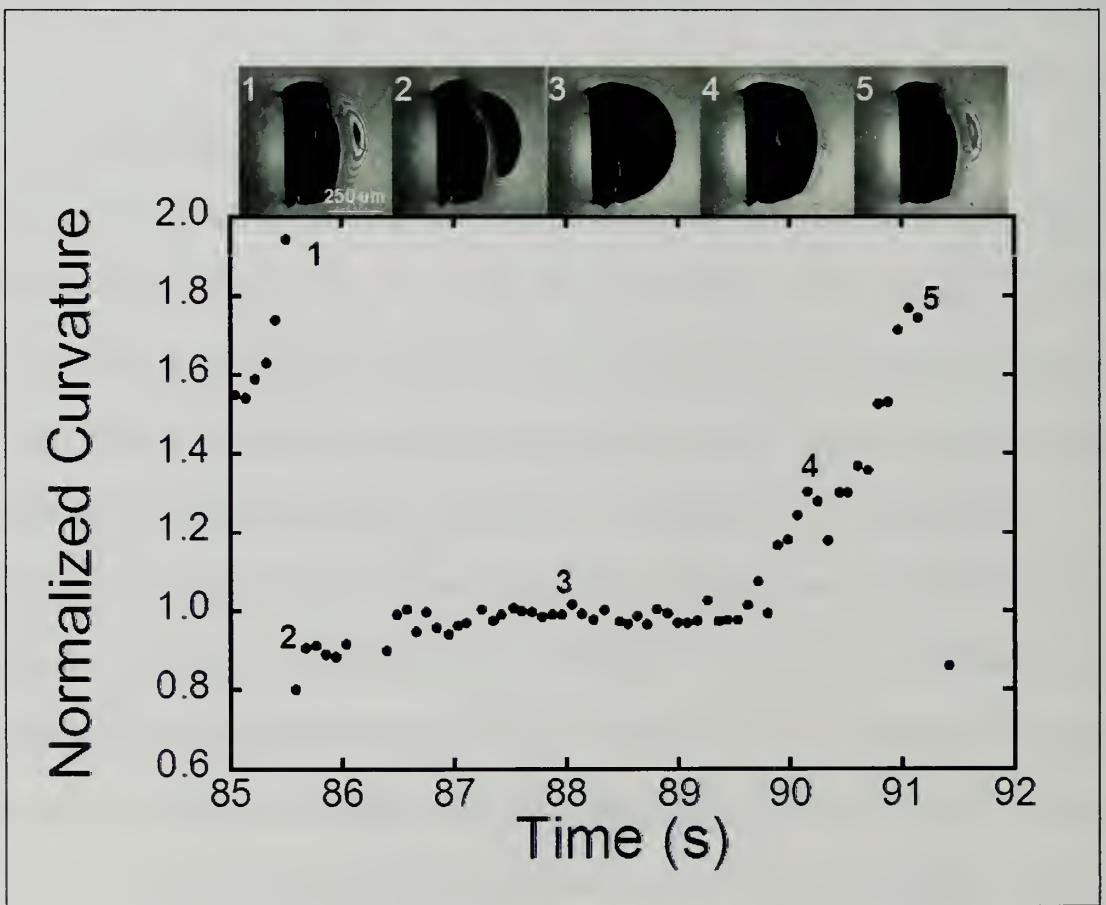

Figure 2.4: Change in continuous curvature from the front of the contact area versus time.

compressive forces developed at the leading edge of the slider, but rise from compressive forces identical to developed by straining a confined elastomeric substrate.

The lateral force rises as the buckle is compressed until the energy stored in the buckle overcomes the critical energy release rate, or adhesion, of the interface. The interface then attaches ahead of the buckle and incorporates a pocket of air. After the buckle attaches, the waves pass along the interface. This process then repeats on a regular basis as lateral displacement proceeds.

To more clearly link the stages of Schallamach wave progression to changes in lateral force, the continuous curvature of the front of the contact area can be normalized by the average curvature during initial shear. A circle can be fit to the continuous front of the image and a curvature can be acquired. This curvature should not be confused with the radius of curvature of the lens and is in fact the curvature of the front of the contact area. This curvature gives insight into how the material is attached to the lens at the leading edge. Figure 2.4 shows this change in contact area curvature for a typical sample where waves form, attach, and pass through the contact area. When buckling occurs the front edge peels back towards the center of contact, thus creating a blunt front edge, or increased curvature. This development is seen in figure 2.4 as the normalized curvature doubles and comes to its peak value of around 2. Attachment causes an immediate drop in this ratio to a value slightly less than the shear value. As the wave passes the contact is restored and the ratio returns quickly to the value of 1. Evaluating the front curvature of the contact area allows for a precise way to evaluate the distinct steps associated with shearing, wave formation, and attachment.

Following Schallamach's discovery, the load, temperature, thickness, and velocity dependence of the waves was evaluated by Barquins *et al*[26-29]. They ranked the factors affecting Schallamach waves by their importance in this order; 1) the adhesive properties, 2) the geometry of contact, 3) the elastic properties of the rubber, 4) load, and 5) temperature[27]. All of these testing parameters play a role in controlling Schallamach waves, the next chapter will evaluate the velocity dependence of Schallamach wave periodicity in terms of materials properties, which had not previously been done.

CHAPTER 3

SCHALLAMACH WAVE PERIODCITY

3.1 MOTIVATION

Schallamach waves proceed at a regular frequency; this is visible in Figure 2.3, where the peaks or attachment points repeat on a regular basis. This length scale should be accounted for when designing a topographically patterned soft surface. Therefore it is critical to fully understand this Schallamach wave length scale, a friction induced surface pattern, and relate that to measurable properties of the sliding interface (i.e. material properties). While work has been done since Schallamach's discovery of detachment waves, there is no fundamental relationship between the periodicity of the waves (λ) and material properties (e.g. the interfacial adhesion (G_c), the complex modulus (E*)). Our goal is to relate Schallamach wave periodicity to materials properties to understand the length scale of this frictionally induced surface pattern.

3.2 INTERFACIAL ADHESION

Adhesive forces between two surfaces create contact areas larger than those predicted by Hertzian mechanics and also require energy to separate two surfaces. Interfacial adhesion is the measure of attractive forces between two surfaces and is a material property. A rigorous analysis of the adhesion energy can be calculated using equation 2.1. This equation can be used to evaluate the strain energy release rate (G) at various steps during a normal contact adhesion test. Plotting G versus contact radius (a) one can calculate the critical energy release rate or the interfacial adhesion at the point where the critical contact area during separation where crack propagation is unstable (a_c). Upon reaching a critical contact radius during separation (a_c), separation becomes

unstable. For materials that obey the assumptions of the JKR theory[13], a_c occurs at the maximum tensile ($P_{max,T}$) (tension is associated with positive values, while compression is associated with negative values) force during separation, such that:

$$G_c = \frac{2P_{max,T}}{3\pi R}. \qquad 3.1[13]$$

3.3 EXPERIMENTAL APPROACH

To accomplish our goal, we evaluate the sliding of a rigid lens on a soft elastomeric substrate. To quantify the materials properties and the frictional response, sliding frictional experiments, contact adhesion test, and dynamical mechanical analysis has been performed on the soft elastomeric substrates. The full details of the experimental techniques and sample preparation follow.

A custom instrument was developed in order to quantify the frictional response. A schematic is shown in figure 3.1. In short, a near-frictionless cantilever containing a 50-gram load cell (Sensotec) holds a slider in contact with a flat substrate under a fixed normal load ranging from 10 to 20 mN. The substrate is rigidly fixed to a translating stage of an inverted microscope, Axiovert 200M (Ziess), which is used to image the contact area. The automated translating stage controls the lateral translation velocity through the use of a program developed using National Instruments LabVIEW software. Displacement, lateral force, and the contact area images are recorded at 4 Hz throughout a sliding experiment.

Adhesion measurements were made using a custom built contact adhesion test shown in figure 3.2. A hemispherical lens (R = 5mm, purchased from Edmund Optics) is

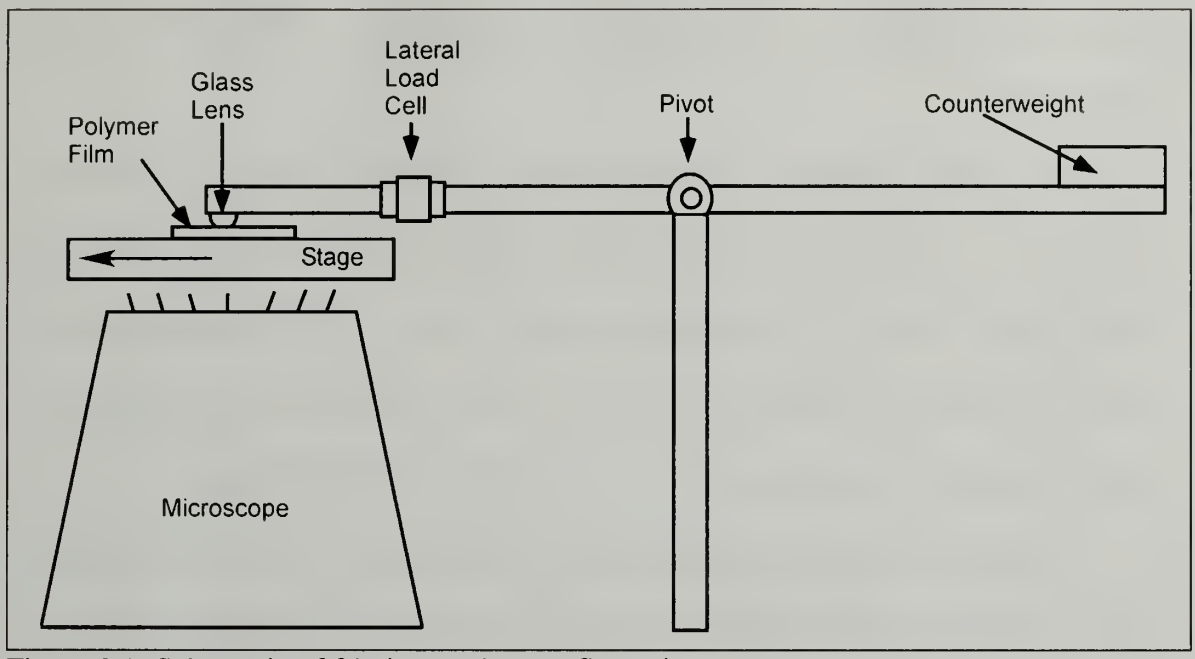

Figure 3.1: Schematic of friction testing configuration.

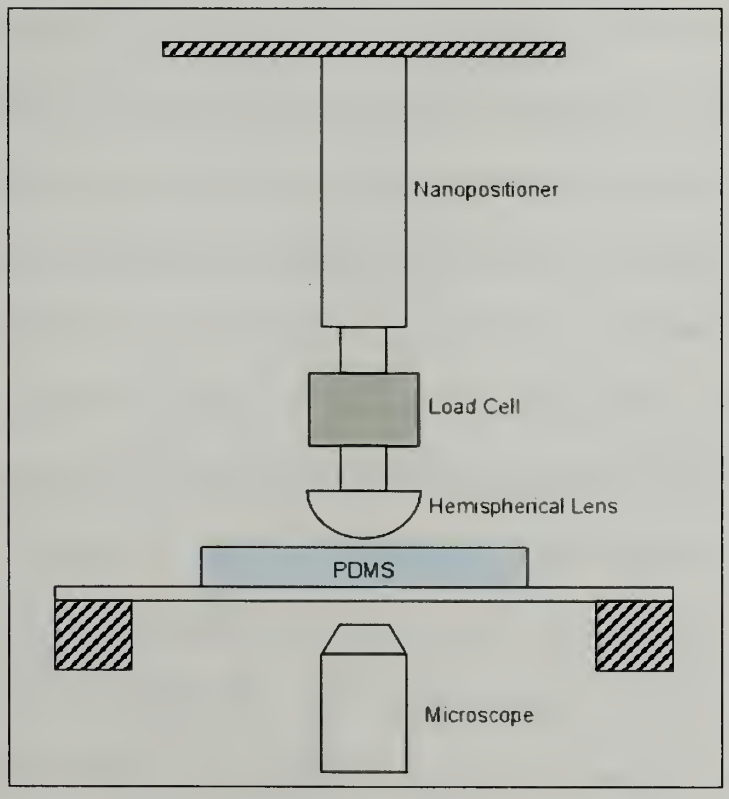

Figure 3.2: Schematic of contact adhesion test.

mounted to a load cell that is attached to a nanopositioner, which provides vertical displacement.

The PDMS substrate is rigidly fixed to a translating stage of an inverted microscope, Axiovert 200M (Zeiss), which is used to image the contact area. The nanopositioner is used to bring the lens in contact with the PDMS substrate at a fixed velocity of 1μm/s until a compressive force of 1 mN is achieved. The nanopositioner is then retracted at the following velocities: 1, 5, 10, 21, 42, 84, 250, 500μm/s.

Complex modulus measurements were made using TA's DMA 2980. Samples were evaluated using tension deformation. The temperature was held fixed at 33° C for all measurements. The amplitude of deformation was fixed at 15 μm and a frequency sweep was conducted. Storage and loss moduli were evaluated at the following frequencies: 0.01, 0.02, 0.03, 0.04, 0.1, 0.16, 0.25, 0.4, 0.63, 1, 1.6, 2.5, 3, 6.3, and 10 Hz.

To establish a relationship between λ and the interfacial and bulk properties of materials, we focused on interfaces of fused silica and cross-linked poly(dimethyl siloxane). The slider was a fused silica hemispherical lens, radius of curvature 5 mm, purchased from Edmunds. The elastomeric substrate was a crosslinked poly(dimethyl siloxane) (PDMS), Dow Corning's Sylgard 184. Varying the ratio of crosslinker to prepolymer was used to control the modulus. The crosslinker to prepolymer weight ratio used in this set of experiments was 1 to 10, 11, 13, 15, and 20. This was done intentionally to vary the moduli of the substrates; the results are shown in figure 3.3. All samples were cured at 70° Celsius for 24 hours. The weight of each sample, before curing, was used to ensure uniformity of film thickness (~ 1 mm) each sample had the same weight (~2 grams). After curing, the samples were swollen in hexane that was

changed twice at 24-hour intervals. Swelling minimizes the amount of un-crosslinked polymer chains at the surface, which can provide lubrication between the slider and the substrate and complicate reproducibility.

The samples were dried for one day at 23° C and one day at 70° C in an oven. After drying, the films were mounted on a clean glass slide and tested. All sample preparation and frictional testing was done in a semi-cleanroom environment to minimize contamination from dust.

3.4 Results

The periodicity of the Schallamach wave (λ) is defined as the distance translated by the stage between subsequent buckle attachments to the slider at the leading edge. Experimentally this distance is the distance between peaks in figure 3.4. This length scale varies as a function of testing parameters and material properties. For example, in figure 3.5 this buckle periodicity was plotted versus testing velocity for all of the substrates.

Presented in Figure 3.6 are the results from contact adhesion tests on all of the samples. The results indicate that the interfacial adhesion shows similar velocity dependence to buckle periodicity in the frictional experiments over the range of velocities tested.

The results from dynamic mechanical analysis are shown in figure 3.7. The modulus results indicate that the in all of the samples the storage modulus dictates the complex modulus and has a negligible velocity dependence. The loss modulus shows a one-third dependence on velocity but it is an order of magnitude smaller than the storage modulus and does not significantly affect the complex modulus.

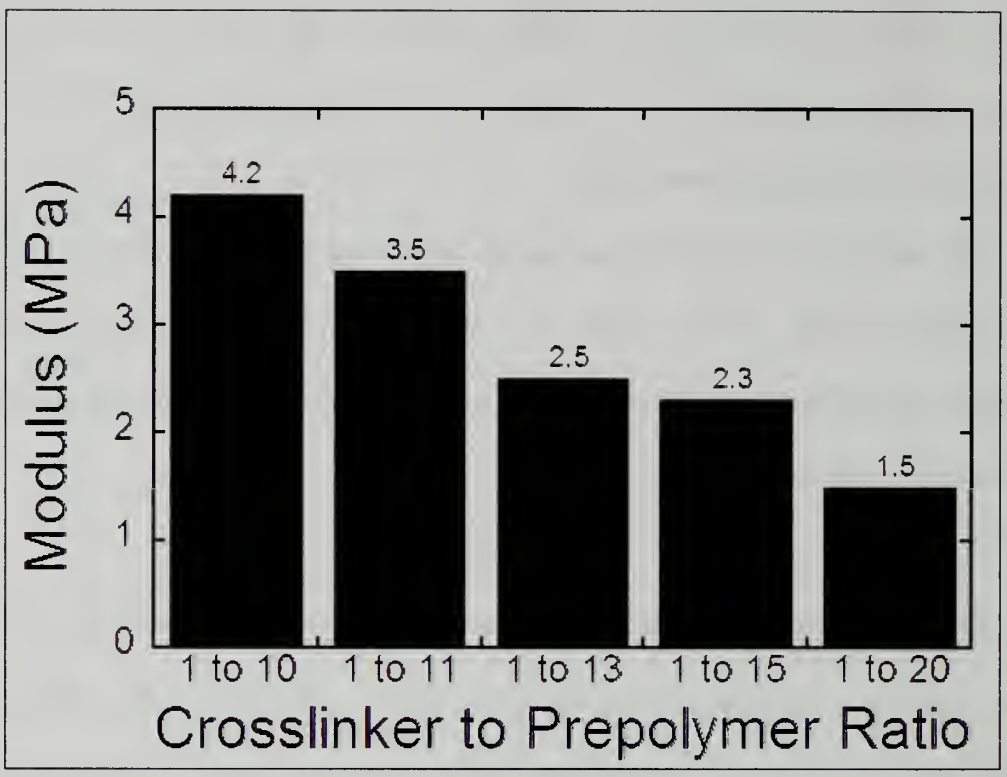

Figure 3.3: Moduli as a function of crosslinker to prepolymer ratio.

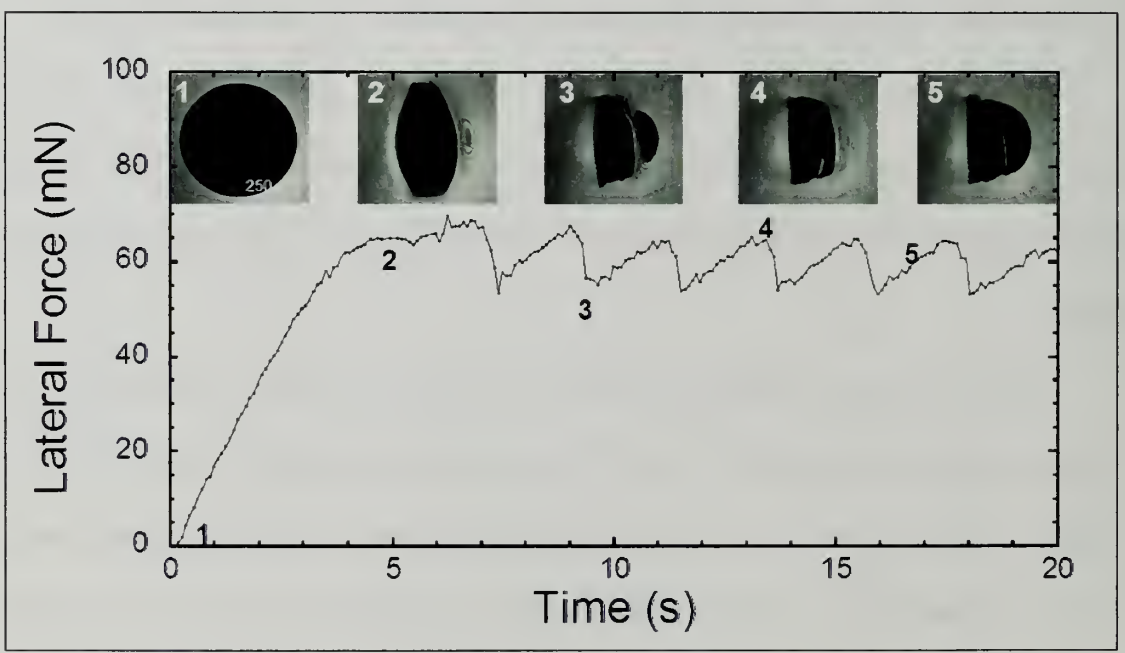

Figure 3.4: Typical lateral force versus time curve for samples with Schallamach waves.

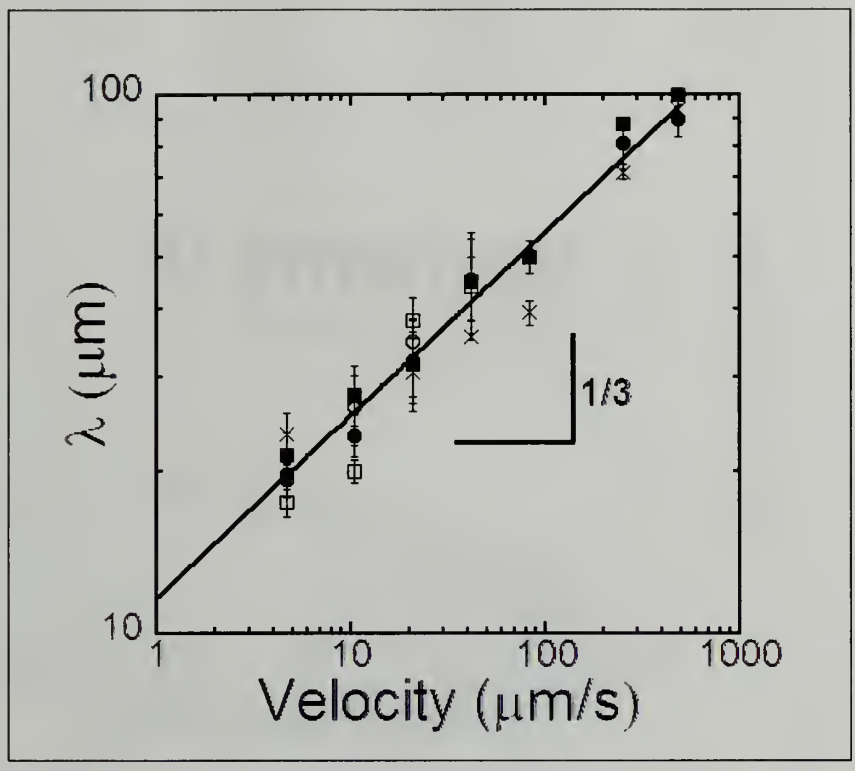

Figure 3.5: Buckle periodicity (λ) versus velocity. (○ – E*=1.7 MPa, □ - E*=1.6 MPa, ● – E*=1.3 MPa, ■ – E*=0.9MPa, x – E*=0.6MPa (E* at ω = 0.3 Hz), R=5mm)

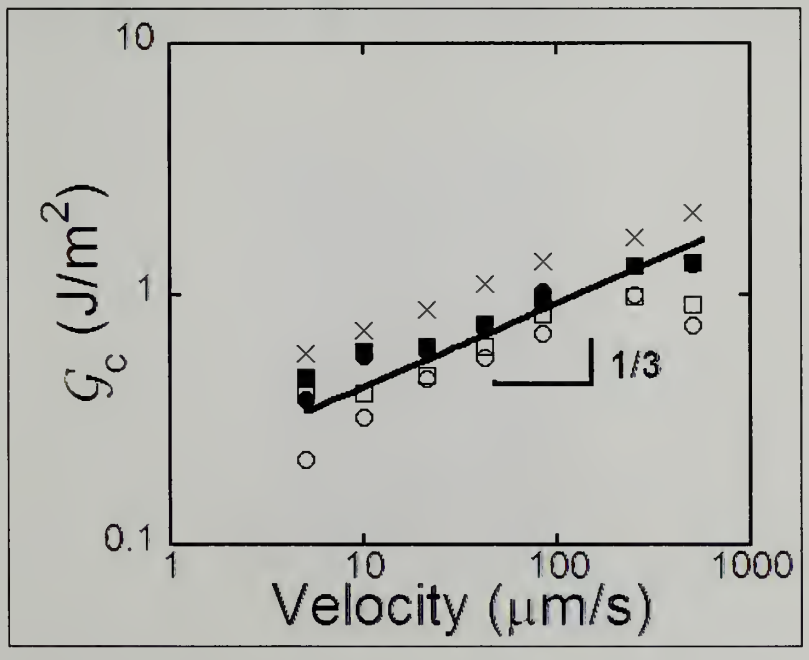

Figure 3.6: Interfacial adhesion (G_c) versus velocity. (○ – E*=1.7 MPa, □ - E*=1.6 MPa, ● – E*=1.3 MPa, ■ – E*=0.9MPa, x – E*=0.6MPa (E* at ω = 0.3 Hz), R=5mm)

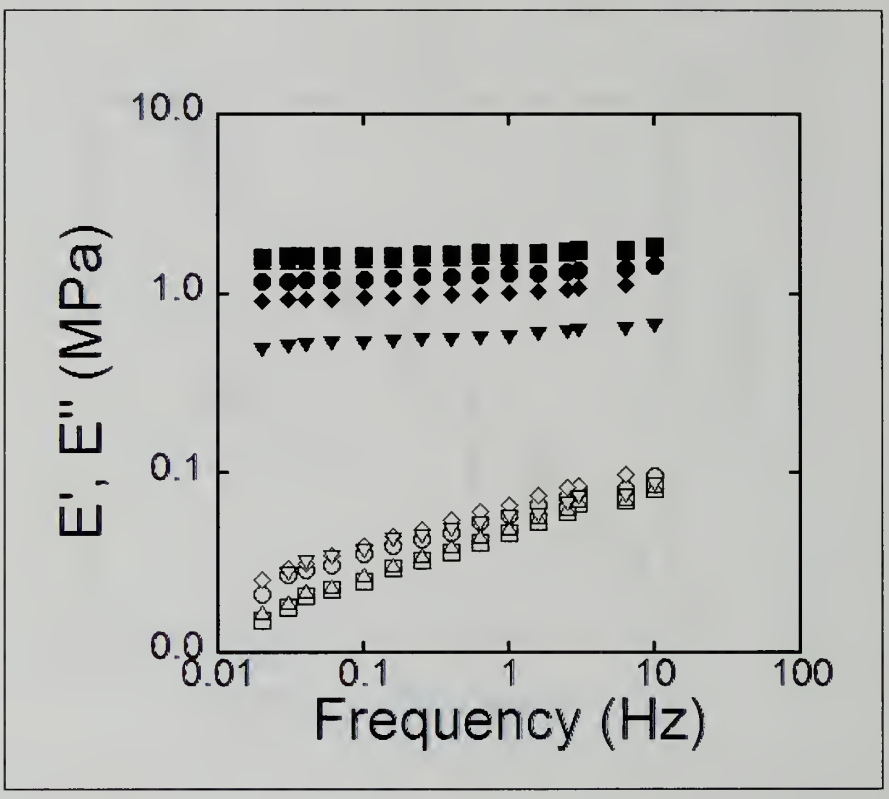

Figure 3.7: Storage (E') (closed symbols) and loss (E") (open symbols) modulus versus frequency. (Crosslinker to prepolymer ratios of ■ – 1to10, ▲-1to11, ●-1to13, ♦-1to15, and ▼-1to20)

We combine the results of the three different measurement techniques and show how the periodicity depends on interfacial adhesion (3.8) and complex modulus (3.9).

3.5 Discussion

To understand the factors defining buckle periodicity, we consider the transitions of a single wave. Initially, the interface is sheared and the stress and strain at the leading edge of the contact area rises (figure 3.10(a)). At a critical stress, the surface buckles in front of the slider in the direction of travel. At a critical stress and strain value the buckle attaches and propagates through the interface, reliving stress and strain. This process repeats in a cyclic manner as translation proceeds. Rather than considering stress and strain as a function of time, we plot stress versus strain to explain which material properties control the rise and fall of stress and strain, related to the periodicity of Schallamach waves (figure 3.10(b)). First, the slope of this plot is determined by the complex modulus of the elastomer. This relation is completely analogous to the complex modulus ultimately determines what strain is required to achieve a specific stress. The magnitude of the maximum strain achieved prior to buckle attachment to the slider is controlled by the critical stress for interfacial separation, which is controlled by the adhesion energy, $\mathcal{G}_c$.

The buckle periodicity (λ) is proportional to the change in strain ($\Delta\varepsilon = \varepsilon_{max} - \varepsilon_{min}$) times the width over which the peel occurs, 2a.The minimum strain, ε_{min}, is nearly zero for the newly attached interface after wave passage. The maximum strain, ε_{max} , is the strain at which the interface peels is proportional to interfacial adhesion ($\mathcal{G}_c$) over the product of the modulus of the elastic substrate (E*) times the sliding contact width (2a).

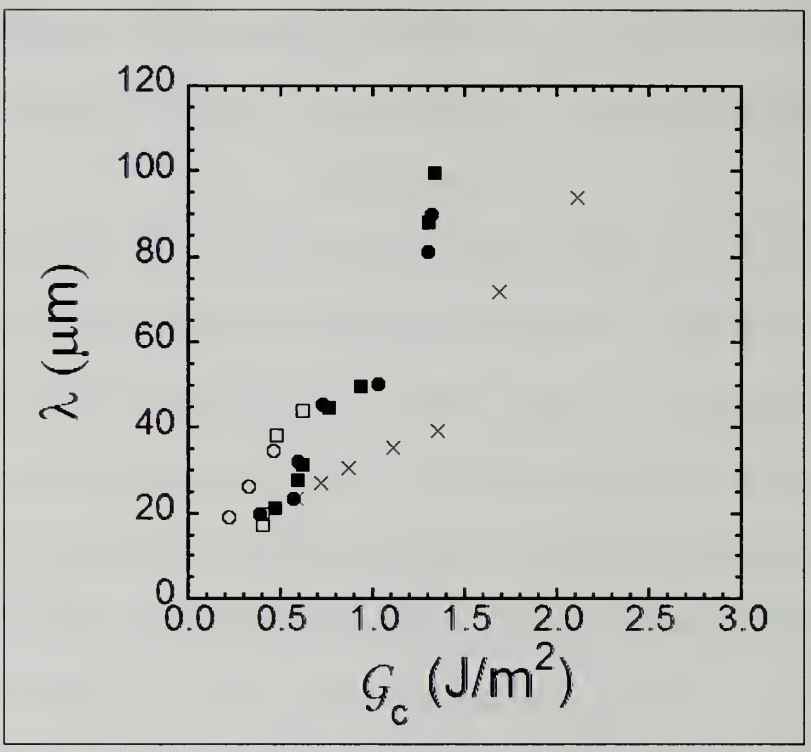

Figure 3.8: Buckle periodicity (λ) versus interfacial adhesion (G_c). (○ – E*=1.7 MPa, □ - E*=1.6 MPa, ● – E*=1.3 MPa, ■ – E*=0.9MPa, x – E*=0.6MPa (E* at ω = 0.3 Hz), R=5mm)

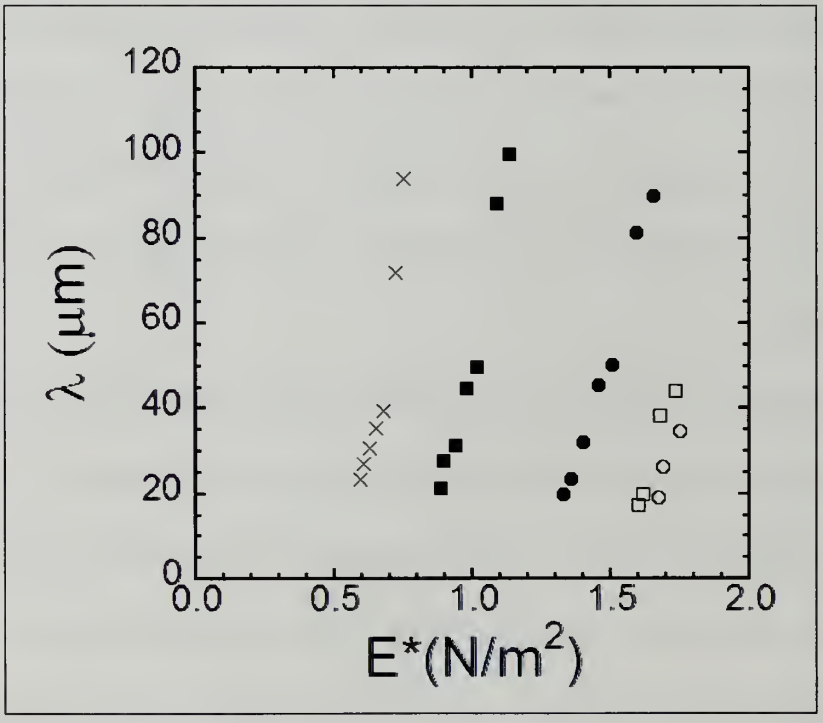

Figure 3.9: Buckle periodicity (λ) versus complex modulus (E*). (○ – E*=1.7 MPa, □ - E*=1.6 MPa, ● – E*=1.3 MPa, ■ – E*=0.9MPa, x – E*=0.6MPa (E* at ω = 0.3 Hz), R=5mm)

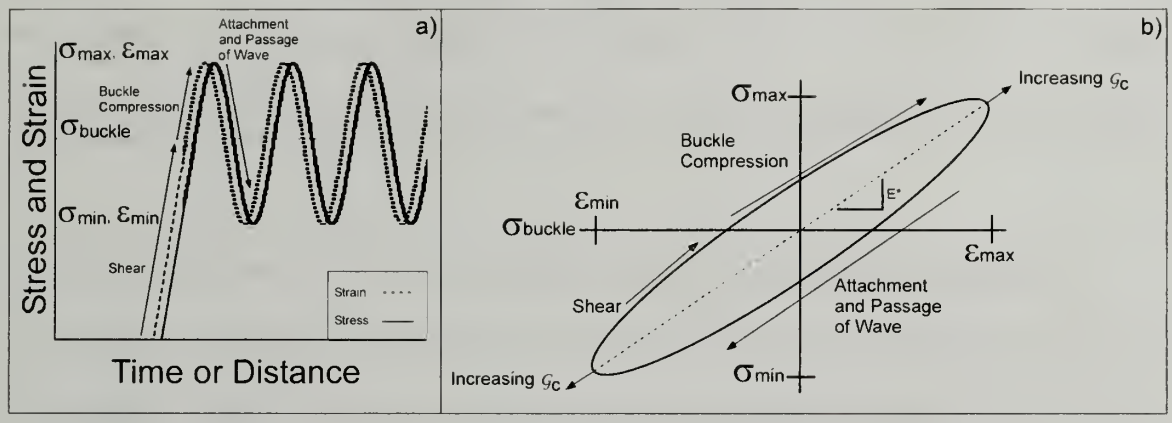

Figure 3.10: a) Schematic of stress and strain versus time or distance for Schallamach waves b) Cyclical representation of a Schallamach wave.

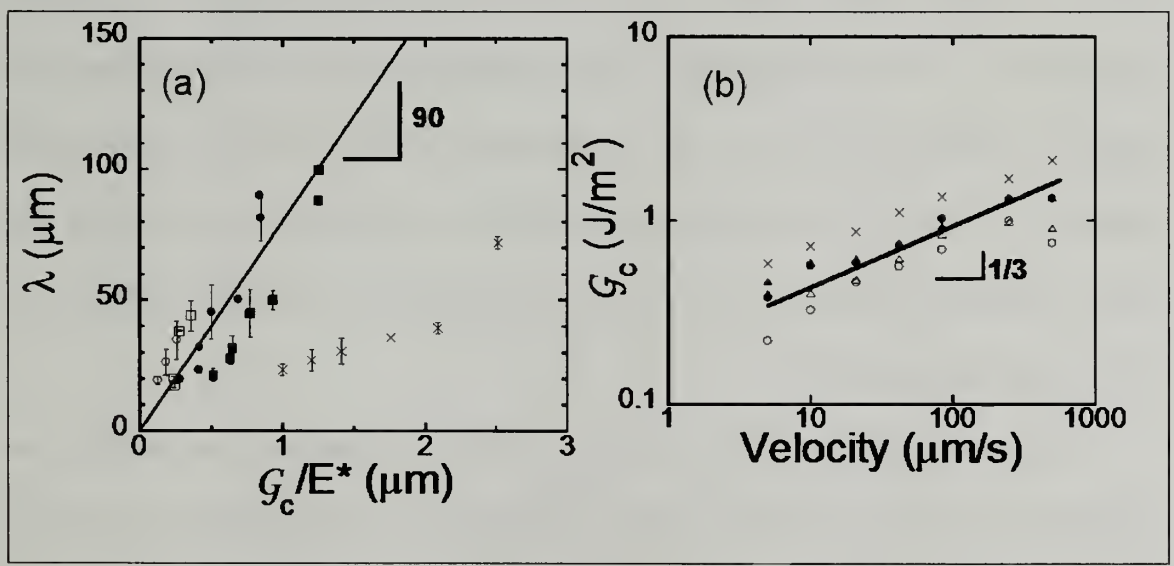

Figure 3.11: (a) Buckle periodicity (λ) versus $\mathcal{G}_c$ over E* (b) $\mathcal{G}_c$ (mode I) versus velocity. (○ – E*=1.7 MPa, Δ - E*=1.6 MPa, ● – E*=1.3 MPa, ▲ – E*=0.9MPa, x – E*=0.6MPa (E* at ω = 0.3 Hz), R=5mm) Reproduced from Rand *et al.*[30]

Therefore $\lambda = (\beta)(\mathcal{G}_c / E^*)$. Traditionally, the interfacial material property related to frictional mechanisms is the critical energy release rate ($\mathcal{G}_c$) or interfacial adhesion under mode II failure. For Schallamach waves, the primary mode of interfacial failure is mode I.

This change in failure mode is due to a peeling moment dictated by the geometry of the buckled surface. To pass a wave across the interface, the applied energy release rate ($\mathcal{G}$) at the leading edge of the wave must exceed or equal the critical energy release rate, $\mathcal{G}_c$, or the energy per unit area required to separate the interface.

Accordingly, λ is related to the balance of $\mathcal{G}_c$ and E* (figure 3.11(a)). This ratio defines a material length scale, whose velocity dependence dictates the velocity dependence of λ. This relationship clearly demonstrates that the velocity-dependent nature of Schallamach waves is not independently related to the bulk viscoelastic properties (E*) or the velocity dependent interfacial properties ($\mathcal{G}_c$), but rather the velocity dependence of the ratio $\mathcal{G}_c/E^*$. For many materials the velocity dependence of $\mathcal{G}_c$ or E* may dominate the process.

For our materials, E* is essentially velocity or frequency independent, as measured by dynamic mechanical analysis (DMA), but $\mathcal{G}_c$ is dependent upon velocity (figure 3.11(b)). $\mathcal{G}_c$ was measured using contact adhesion tests based on the theory of Johnson, Kendall, and Roberts[13, 31]. This velocity dependence of $\mathcal{G}_c$, for PDMS-PDMS and PDMS-glass interfaces, has been reported previously by many researchers and is largely related to the rate of bond dissociation[32, 33]. Therefore, for this material interface, the velocity dependence of λ is not related to the bulk viscoelasticity, but rather to the frequency dependence of the interfacial strength.

3.6 Summary

The deconvolution of the interfacial and bulk contributions to Schallamach waves suggests interesting predictions. If materials are appropriately designed, the velocity dependence of $\mathcal{G}_c$ could be tuned to relate to the velocity dependence of E*, such that the friction of a viscoelastic material would be independent of velocity. Second, the relationship of λ to $\mathcal{G}_c$ /E* suggests that the periodicity of Schallamach waves will quickly approach nanometer length scales for more rigid materials. Direct observation of theses waves will be challenging, but their impact on wear mechanisms would be extremely relevant to the design of materials.

In this study, experiments to understand the fundamentals of Schallamach waves were conducted. It was found that the leading edge curvature provides a better understanding of the distinct events involved with Schallamach wave formation, attachment, and passage. The balance of interfacial and bulk contributions, as described by the material length scale $\mathcal{G}$c /E*, was related to the periodicity (λ) of Schallamach waves. This deconvolution was introduced through the analysis of Schallamach waves in terms of the stress-strain cycles at the leading edge of the interface. This insight leads to interesting predictions that will impact material design for the wide range of applications where Schallamach waves are observed or anticipated.

3.7 Acknowledgements

This work was supported by the NSF Career Award No. DMR-0349078, NSF-MRSEC at the University of Massachusetts, and Army Research Laboratory Center of Excellence at the University of Massachusetts.

CHAPTER 4

FRICTIONAL MANIPULATION THROUGH A SINGLE LINE DEFECT

4.1 INTRODUCTION

In the last chapter we evaluated the length scales associated with Schallamach waves or naturally occurring frictionally induced patterns that occur at the surface. In addition to these naturally occurring patterns, we were interested in studying the effect of patterns already on the surface of the sliding interface. In order to evaluate a complex pattern covering the entire surface, we first began by evaluating the effects of a single feature or defect. In this study, we evaluated the effect of a single incision or defect on the frictional response of the sliding interface composed of a rigid surface and a soft elastomeric surface.

The use of patterned surfaces has gained attention recently as science tries to imitate nature. Many authors have studied the gecko's foot in order to understand how to mimic its enhanced adhesion[3, 4, 34, 35]. Biological structures such as the setae and spatulae that decorate gecko's foot have been the inspiration for synthetic structures with similarly patterned features to provide enhanced adhesion control (figure 4.1(b-d)).[2-8, 36-39] While most research has focused on adhesion enhancement under normal loading, the role of patterns or discrete structures under shear loading or sliding is also critical for practical application of these surfaces.[40]

Work by Majidi *et al* on microfiber arrays of polypropylene showed that fibril arrays showed an enhancement in static coefficient of friction compared to a flat surface[40]. Contrary to these results, Varenberg and Gorb presented results on soft

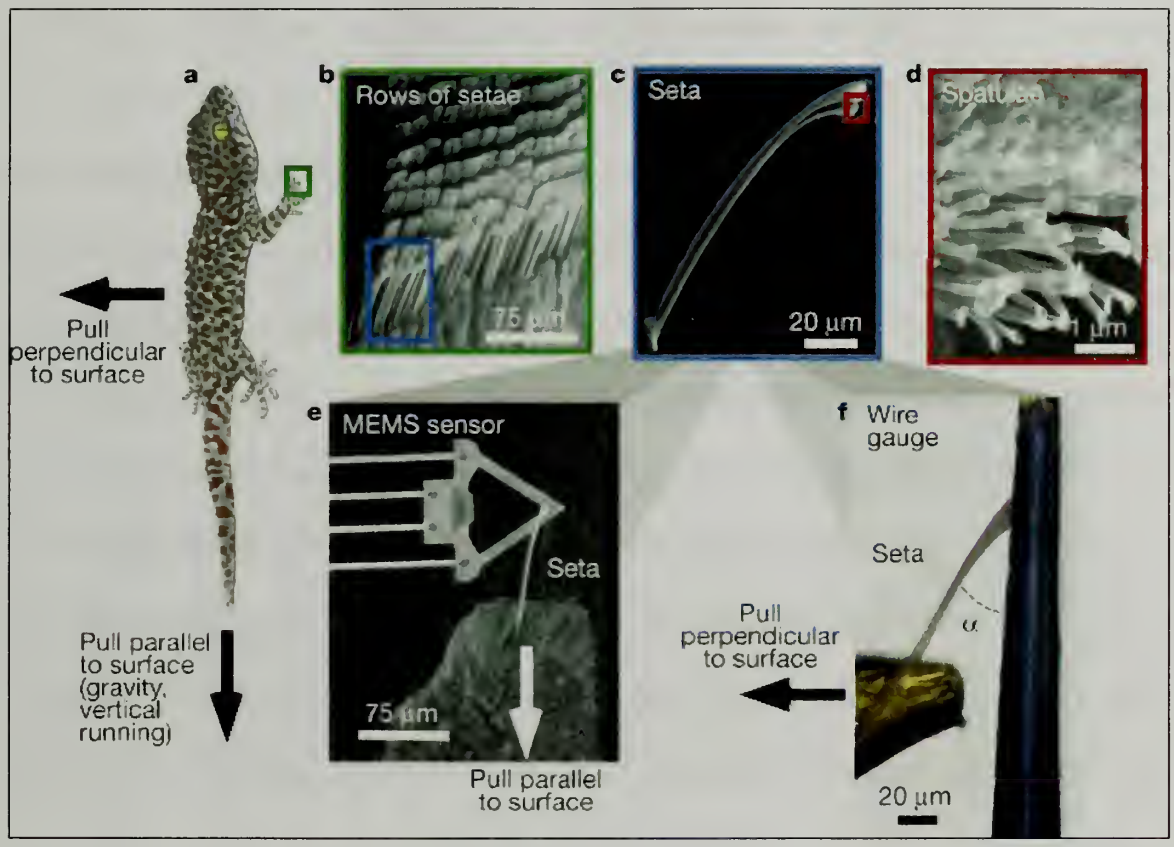

Figure 4.1: a) Gecko and the forces it undergoes b) rows of setae c) single seta d) spatulae e) and f) single seta attached to force gauges. Reproduced from Autumn *et al*[2]

mushroom shaped fibrillar structures that showed a dramatic decrease in the sliding frictional force and a change in the frictional mechanism [38]. Majidi's results are a result of an increase in actual contact area due to the more compliant and conforming surface, which causes an increase in the frictional force required for sliding. The surface is more compliant laterally, but ploughing and increased adhesion counteract any decrease in friction as a result from the more laterally compliant surface. Varenberg and Gorb attribute their results to a decrease in the sliding contact area and increased lateral compliance associated with the fibrillar structures. Additionally, Niederegger *et al* evaluated the friction of projections from a spider's legs[41]. They noticed that the friction was anisotropic due to sticky pads located on one side of the hair-like structures. They noted that structural and adhesive differences seem to account for the spider enhanced friction in one direction leading to this anisotropy.

While work has been done on synthetic and natural structures the data may be convoluted by two separate events: 1) changes in contact area 2) changes in lateral compliance. It is critical to understand the frictional response of these materials in order to fully understand their potential use in real world applications. It is also critical to start from the macro scale and progressively work towards smaller scales, fully understanding this transition will help the future development of smart adhesive materials that may undergo tangential loadings and also smart frictional surfaces. In subsequent chapters, we discuss transferring the understanding of a single line defect to multiple defects to provide guiding principles in the design of protective coatings.

4.2 MOTIVATING PRINCIPLES

When a slider moves along a surface, the slider not only acts on a volume of material below the contact area but also in front of and behind the sliding contact area. Schallamach indicated that a compressive zone develops in front of the slider in the direction of travel and a tensile zone trailing the slider[12]. Figure 4.2(a) shows the theoretical strain distribution created at the surface of a soft elastomer by a rigid lens. This is confirmed by the experimental results shown in figure 4.2(b) where the lattice drawn on the surface of the soft elastomer confirms the stress transitions from compression to tension in the contact area. It also clearly proves that strain and thus stress is exerted outside of the contact area.

From the work of Schallamach (figure 4.2 (b)), it is evident that the stress distribution created by a rigid slider at the surface of a soft elastomer exceeds outside of the contact area and eventually disappears at a certain distance away from the contact area. Cutting or patterning a topographical feature at the surface can interrupt the transfer of stress at the surface and in the bulk. For example, a simple cut would relive the tensile stress at the trailing edge, as tensile forces overcome the adhesion at the interface allowing the trailing portion to separate from the interface and the defect to open. A cut (assuming the width is negligible) would have no effect in the compressive region of the stress distribution since stress and strain are transmitted under compression.

Cutting or patterning can provide a material surface that appears to be a continuous, but has dramatically lower frictional properties caused by stress transfer discontinuities at the surface. In this case the surface is broken up into strips separated by negligible distances.

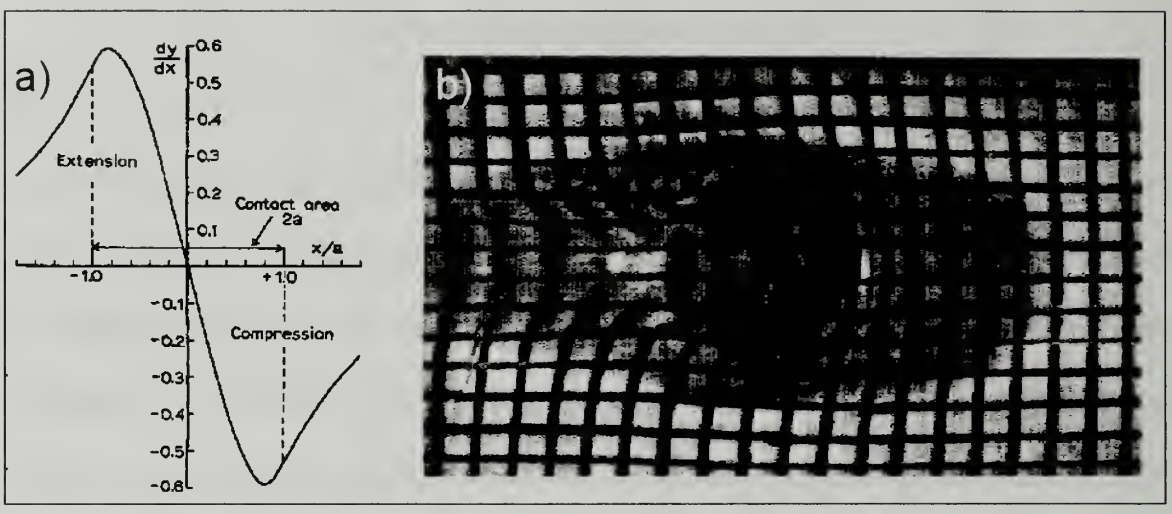

Figure 4.2 a) Theoretical strain distribution at the surface of a soft elastomer created by a sliding rigid hemisphere b) Sliding contact area of a rigid hemisphere sliding on a soft elastomer that was marked with a grid to evaluate strain. Reproduced from Schallamach[12].

4.3 Experimental Approach

To test the effect of a cut or defect in the sliding interface, two testing geometries were used to evaluate a transient cut and one static with regards to the sliding interface. To explore the effect of a defect under various conditions the shear modulus was varied, the thickness was varied for one modulus, and the applied load was varied for one modulus.

Using the custom-built sliding friction instrument described previously in chapter 3, two testing geometries were used to study the friction of soft, elastomeric surfaces with line defects (figure 4.3). In the first, a polished fused silica glass hemisphere (R, radius of curvature, = 5mm) was translated in contact with a flat, crosslinked polydimethylsiloxane (PDMS) (Dow Corning's Sylgard® 184) substrate (figure 4.3(a)). The thicknesses of the substrates were 1mm or 0.4mm, as indicated in the appropriate results. All PDMS substrates were swollen in hexane for two days to minimize the number of free chains at the surface. The shear modulus (G) of the substrate was varied from 0.37, 0.51, to 0.91 MPa by changing the cross-linker to prepolymer ratio 1:10, 1:15, and 1:20 respectively. In the second configuration, PDMS was used as the spherical probe and a fused silica glass slide was used as the flat substrate (figure 4.3(b)). In this configuration the PDMS crosslinker to prepolymer ratios were 1:10 and 1:15 yielding G ~ 1.0 MPa and 0.65 MPa. The spherical PDMS lenses were cast from a fused silica mold (R = 25mm).

The line defects for both configurations were physical incisions in the PDMS, which were created using a Teflon coated razor blade. In the films, a single defect was made in the center of the sample. For the PDMS lenses, the location of the defect relative

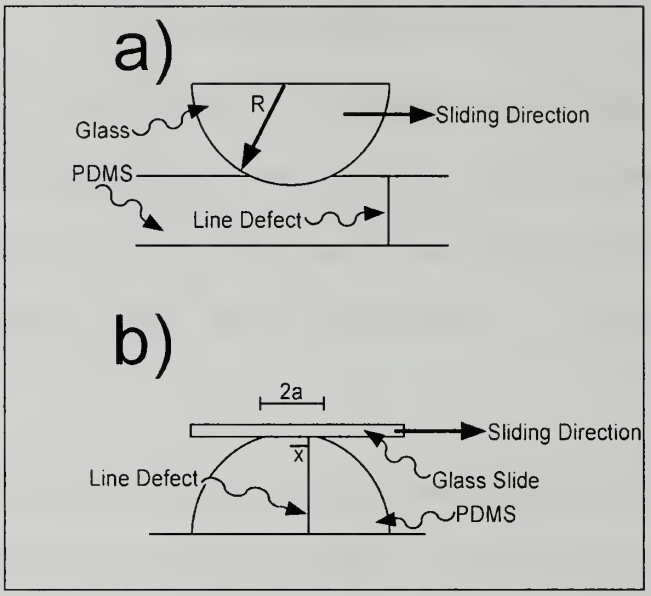

Figure 4.3: a) Glass lens sliding on PDMS film with line defect, b)Glass slide sliding on PDMS lens with line defect. Reproduced from Rand and Crosby[42].

to probe's apex was varied systematically. This position is indicated as x in figure 4.3(b). All defects were made through the PDMS thickness.

Lateral sliding force was measured while applying a constant normal force (P) (~18, 30, and 40 mN for the PDMS films and ~23, 26, and 30 mN for the PDMS lenses). The lateral velocity (v) was fixed at 5μm/s. The interfacial contact area was imaged through an inverted microscope allowing for the evaluation of changes in the contact area and the associated frictional mechanism by which the two surfaces displaced. The results represent the statistical mean of multiple runs on the same sample under the same conditions. We measured the adhesion energy ($\mathcal{G}_c$) of PDMS/fused silica interface using an axi-symmetric probe contact adhesion test.[13, 31] The shear modulus (G) of each substrate was evaluated through the use of contact mechanics.[43] The shear modulus (G) was calculated during the initial shearing of the interface using the following equation

$$\frac{\partial F}{\partial \delta} = \frac{8Ga}{3(1-\nu)}, \qquad (4.1)[43]$$

where $\partial F/\partial \delta$ is the initial slope of the sliding force displacement curve or the tangential stiffness, a is the initial contact radius, and ν is the Poisson's ratio of the elastomeric surface.

4.4 Results

Representative data for a glass probe sliding over a defect-free PDMS substrate is shown in figure 4.4(a). Prior to shearing the PDMS-glass interface, a circular contact area is established (image 1, figure 4.4) whose dimension is determined by the contact conditions and materials properties at the interface (i.e. lens curvature, adhesion, elastic moduli, and applied normal load) as dictated by equation 2.1. Upon shearing, the shear

modulus (G) of the substrate and the contact radius (a) dictate the initial slope of the force-distance curve. Relative translation, or sliding, proceeds by the formation and passage of Schallamach waves (figure 4.4a) for these materials, except at the highest normal loads. This transition from Schallamach waves to stick-slip at increased normal loadings has been previously reported by Barquins and Roberts.[29]

For substrates with line defects, the average lateral force is unaffected until the defect encounters a given position within the sliding interfacial area (figure 4.4b). At this point, the lateral force decreases instantaneously and recovers as the sliding interface moves away from the defect. The trend associated with this force drop, not the magnitude, is universal for a variety of materials and contact conditions and corresponds to the defect's transition through the interfacial area. The maximum force drop due to the defect is plotted for various materials and conditions in figure 4.5, which indicates that this reduction can be controlled by materials properties.

In this configuration, defects transition from the leading edge of the interfacial area to the receding edge and the decrease in the lateral force is clearly associated with the defects' position within the sliding interfacial area. To further explore the effect of defect position on the force drop magnitude, we quantified the sliding force for a PDMS probe with a defined defect position sliding across a glass substrate. In this configuration, the defect's position within the sliding interfacial area is stationary (figure 3.4(b) and is quantified by the distance from the center of the probe's apex (x) normalized by the pre-sheared contact radius (a). For these experiments, the lenses were not swollen in hexane to remove free chains; hence the sliding mechanism is stick-slip not Schallamach waves. Nonetheless, the effect of the line defect is similar to

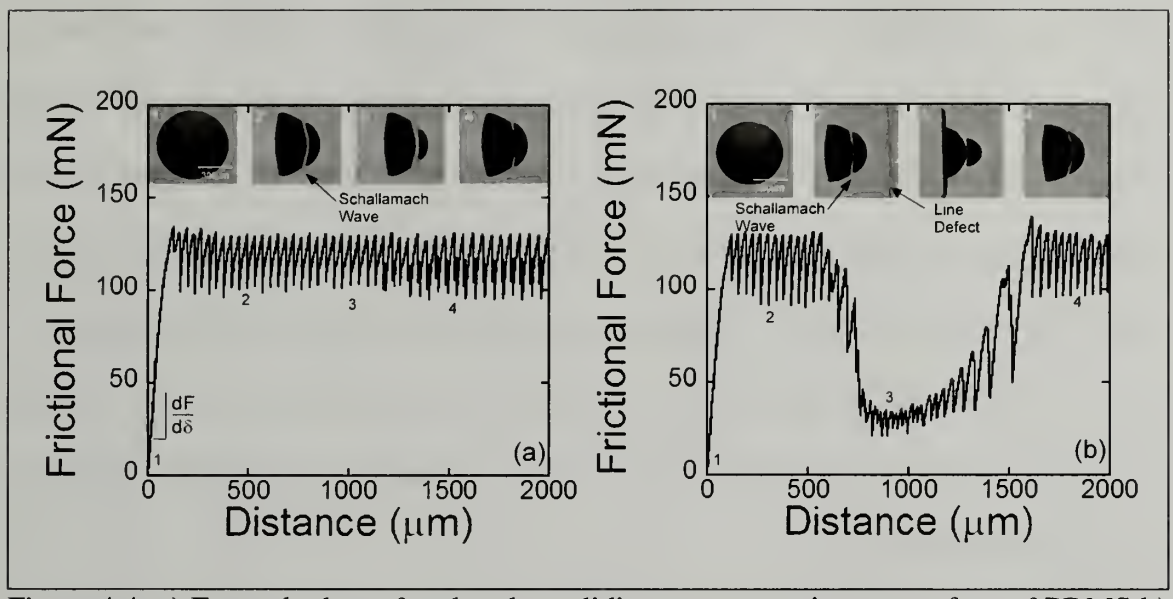

Figure 4.4: a) Example data of a glass lens sliding over a continuous surface of PDMS b) Example data of a glass lens sliding over a line defect in a PDMS film. Reproduced from Rand and Crosby[42].

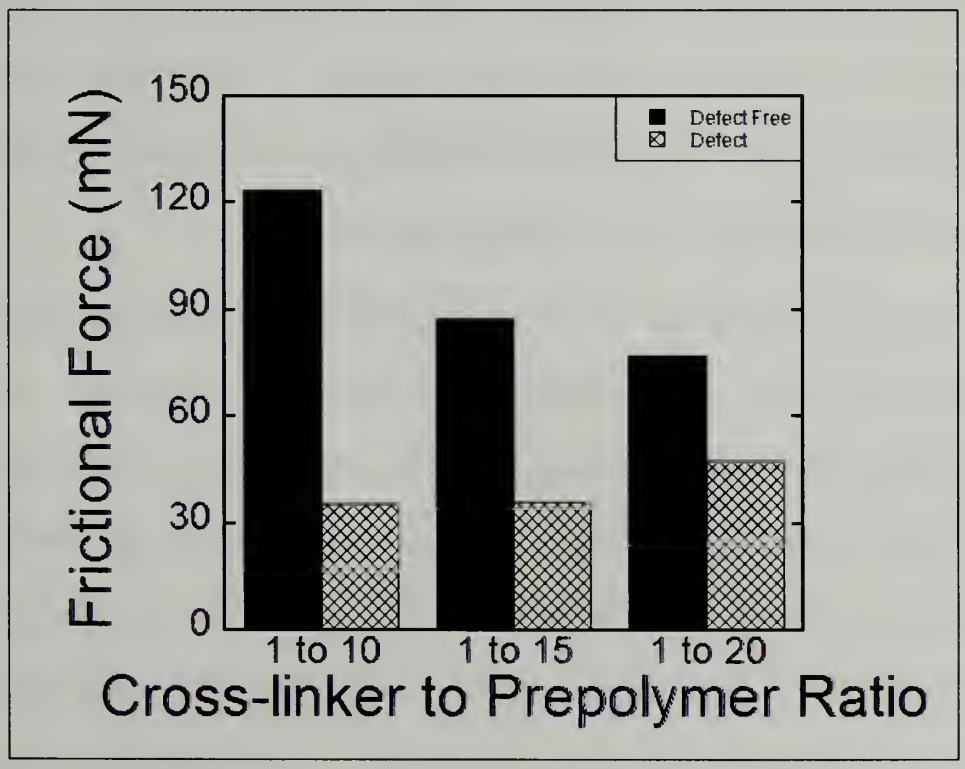

Figure 4.5: Glass lens sliding on PDMS substrates of varying crosslink to prepolymer ratios. R= 5mm, P=18mN, v=5μm/s.

experiments described above. Two representative force-distance curves are presented in figure 4.6(b). The overall response of these two tests is similar, but the magnitude of the force is different. In this test configuration, transient force drops are not observed but rather a continuous progression of stick-slip translation at a reduced force. The position of the defect within the contact zone dictates the magnitude of the average sliding force, which is summarized in figure 4.6(a). The normalized frictional force is the average sliding force for each cut lens divided by the average sliding force for a defect-free lens at the same testing conditions.

These results indicate that the decrease in lateral force begins as the defect position nears $x/a \sim 0$. The sliding force increases as the defect position moves away from the receding edge of the sliding area ($x/a < -1$) and returns to the defect-free lateral force. This data indicates that defects in the leading region ($x/a > 0$) and far away from the contact area play no role in lowering the frictional force, while defects in trailing portion ($-1 < x/a < 0$) significantly decrease the sliding frictional force.

The positional control of the force drop is related to the lateral stress distribution under a sliding interface. As described by Schallamach[12] (see figure 4.2) , the lateral stresses during sliding transition from compressive at the leading edge of the interfacial area to tensile at the trailing edge. Hence, prior to reaching the defect, the lateral force is unaffected since the defect can transfer compressive stresses. Upon reaching the tensile portion of the contact area, the tension opens the defect and relieves the tensile force experienced by the slider, which causes a drastic change in the lateral force required for sliding (figure 4.4(b) and figure 4.6(b)). As the line defect passes the receding edge of the

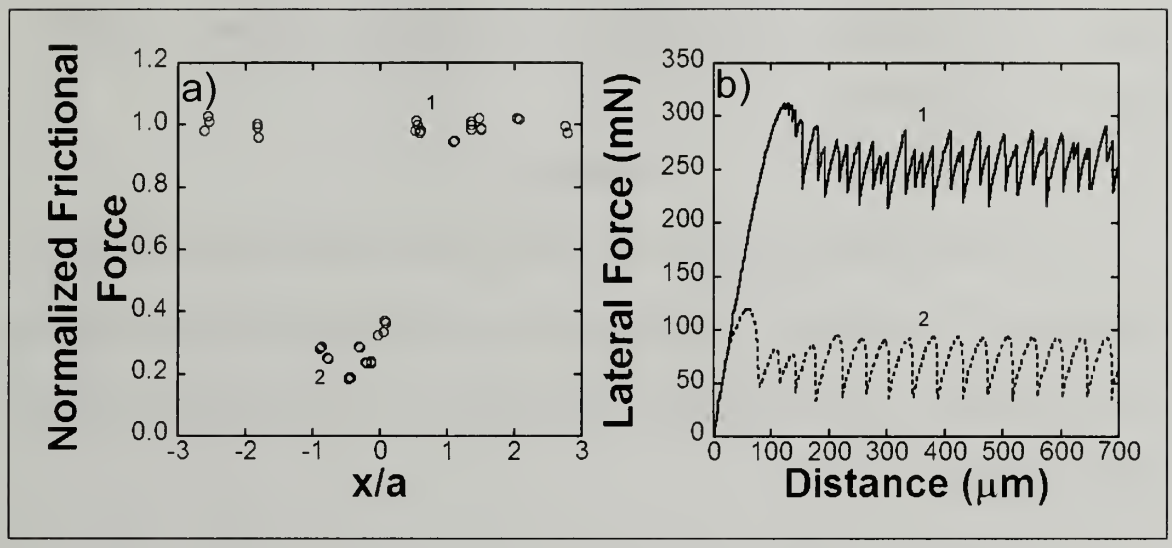

Figure 4.6: a) Normalized frictional force of PDMS lenses defect at various locations (x), b) Examples of the force versus diplacement curves for a defect in compression (1) and one in tension (2). Reproduced from Rand and Crosby[42].

interfacial area, the lateral force rises and reverts to the same value as prior to the sliders interaction with the defect.

4.5 Discussion

To understand the magnitude of the force drop, we consider a standard model for friction $F_s=\tau*A$,[1, 44] where F_s is the sliding force, τ is the interfacial shear strength and A is the true contact area. Assuming incompressibility for the soft material and a circular contact area,[43]

$$A=\left(9\pi k_s^{\,2}\Big/256G^2\right) \tag{4.2}$$

where k_s is the lateral contact stiffness; therefore,

$$F_s=\left(9\pi\tau\cdot k_s^{\,2}\Big/256G^2\right). \tag{4.3}$$

Accordingly, we can define the ratio of sliding force at a defect (F_d) compared to a defect-free region (F_s) as:

$$\frac{F_d}{F_s}=\left(\frac{k_d}{k_s}\right)^2 \tag{4.4}$$

where k_d is the effective lateral contact stiffness at a defect. In this form, τ and G cancel since they are materials properties and the force drop ratio (F_d/F_s) is defined solely by the change in lateral contact stiffness due to the defect. As the line defect experiences tensile stresses that exceed the self-adhesion of the defect's walls and interfacial adhesion, the single sliding contact area splits into two contact regions between which stress transfer is eliminated and the boundary conditions for each area are different than the pre-split area. These changes in the lateral confinement cause significant changes in the lateral stiffness, consequently changing the frictional force.

In equation (4.2), the relation between k_s and A assumes that all length scales (e.g. substrate thickness, h, and distance to a free edge, x) are significantly large relative to $a_s = (A/\pi)^{1/2}$. As the ratios of a_s/h and a_s/x become finite, correction factors must be introduced to correctly describe k_s. For an incompressible material, the tangential stiffness of a single, circular contact region, k_s, can be described as:

$$k_s = \frac{16}{3} G a_s \cdot f_h \cdot f_x \tag{4.5}$$

where f_h and f_x are correction factors that account for finite size effects. Specifically, f_h accounts for lateral confinement introduced when a_s is comparable or larger than the thickness, h, of the soft material.[45, 46] Semi-empirical relationships have been developed to account for these effects under normal loading conditions: [45, 46]

$$f_h = 1 + \frac{4}{3}\left(\frac{a_s}{h}\right) + \frac{4}{3}\left(\frac{a_s}{h}\right)^3 \tag{4.6}$$

and these corrections should be similar under shear loading conditions. The correction factor f_x accounts for changes in lateral constraint when the distance to a free edge is finite. To develop a relationship to describe these edge effects, we conducted sheared contact experiments (i.e. no sliding) at fixed distances between a probe's apex and a free edge (figure 4.7). The correction factor f_x for finite distances to a free edge is measured:

$$f_x = \frac{3\left(\frac{dF}{d\delta}(x)\right)}{16 \cdot a_{eff}(x) \cdot G} \tag{4.7}$$

where $a_{eff} = (A/\pi)^{1/2}$ and $dF/d\delta$ is the measured interfacial tangential stiffness (figure 4.4(a)). Experiments were run on three different modulus samples and the test started with the lens with the center of its apex on the edge of the sample. The lens was sheared,

but never began sliding, to acquire stiffness and contact area. The lens was then lifted from the surface and moved 50 mm from the edge and the experiments was repeated. The results are shown in figure 4.7. It should be noted that the sample with a modulus of 0.57 MPa appears to be shifted from the other sets of data and is most likely due to the lens's apex not being exactly at the edge of PDMS sample for the first measurement. The value of f_x approaches a plateau of unity as the contact position moves away from the unconstrained free edge. This empirical trend can be described as a simple relationship of x/a_{eff}:

$$f_x = 1 - \frac{e^{-x/a_{eff}}}{2}. \tag{4.8}$$

It should be noted that this fit was chosen to take into account the changes in the experimental data; however the exponential function was not chosen to represent a particular physical meaning. This functionality allowed us to have a finite value at x/a=0 and resume unity at a finite distance from an edge. This allowed us to describe these two features noticed in the experimental data.

In addition to the influence of finite size effects on the stiffness of an interface, the splitting of a contact area, as experienced at a sliding incision, also influences stiffness. For multiple contact regions sliding in tandem under fixed displacement conditions, the composite stiffness, k_d, is:

$$k_d = \frac{16}{3} G \sum_{i=1}^{n} a_i \cdot f_{hi} \cdot f_{xi} \tag{4.9}$$

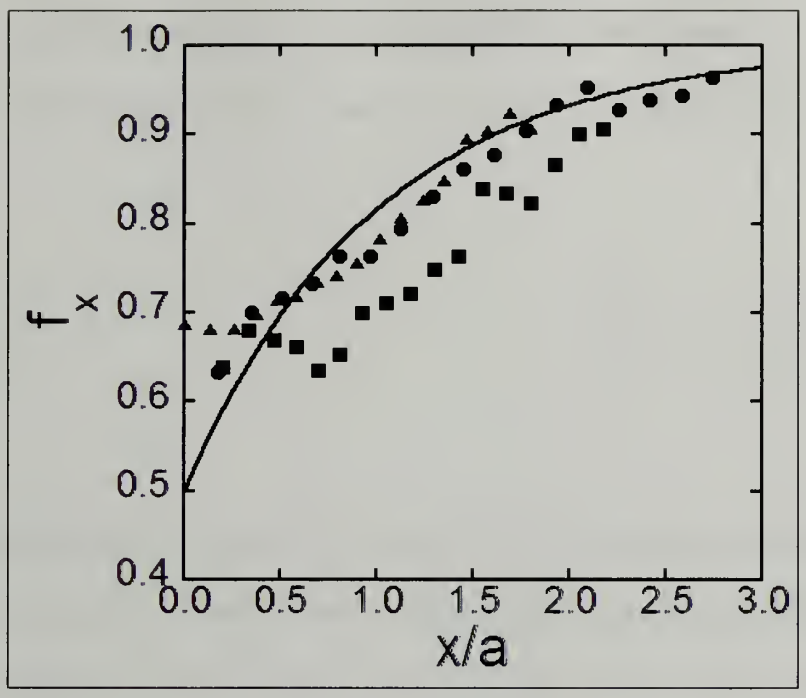

Figure 4.7: Correction factor for finite distance from a free edge (f_x) versus distance from a defect (x) over contact radius (a). (●- G = 0.91 MPa, ■ - G = 0.57 MPa, and ▲ - G = 0.31 MPa)

where a_i is the contact radius of the respective circular region and f_{hi} and f_{xi} are the respective correction factors. Accordingly, we can write an expression for the force drop ratio:

$$\frac{F_d}{F_s} = \frac{A_d}{A_s}\left[\frac{\sum_{i=1}^{n}\left(\frac{a_i}{a_d}\cdot f_{hi}\cdot f_{xi}\right)}{f_h}\right]^2 \qquad (4.10)$$

All expressions above assume that the contact regions are circular, but the general scaling should hold for contact regions that are not circular. In Figure 4.8, we plot F_d/F_s as a function of A_d/A_s, where F_d is the mean minimum sliding force during interaction with the defect and A_d is the mean total area,

$$A_d = \pi\sum_{i=1}^{n} a_i^2 = \pi\cdot {a_d}^2, \qquad (4.11)$$

associated with the minimum sliding force. Trend lines based on equation (4.10) and measured data points are plotted in Figure 4.8. The solid line represents equation (4.10) when f_{hi}, f_{xi}, and f_h equal unity, the case associated with a classical $F=\tau A$ model. It is clear that our data is not represented by this condition. The data for a rigid sliding probe on a flat, PDMS layer is adequately described with one set of values of a_s/h, x/a_{eff}, and a_i/a_d (upper dashed line) and by another set of a_s/h, x/a_{eff}, and a_i/a_d values for the case of the elastomeric lens sliding on the rigid substrate (lower dashed line). These values are not assigned by fitting, but rather correspond to average values measured during testing. An example of a representative measurement of x/a and a_i/a_d is shown in the inset in figure 4.8. These measurements were made by overlaying the contact area at the defect

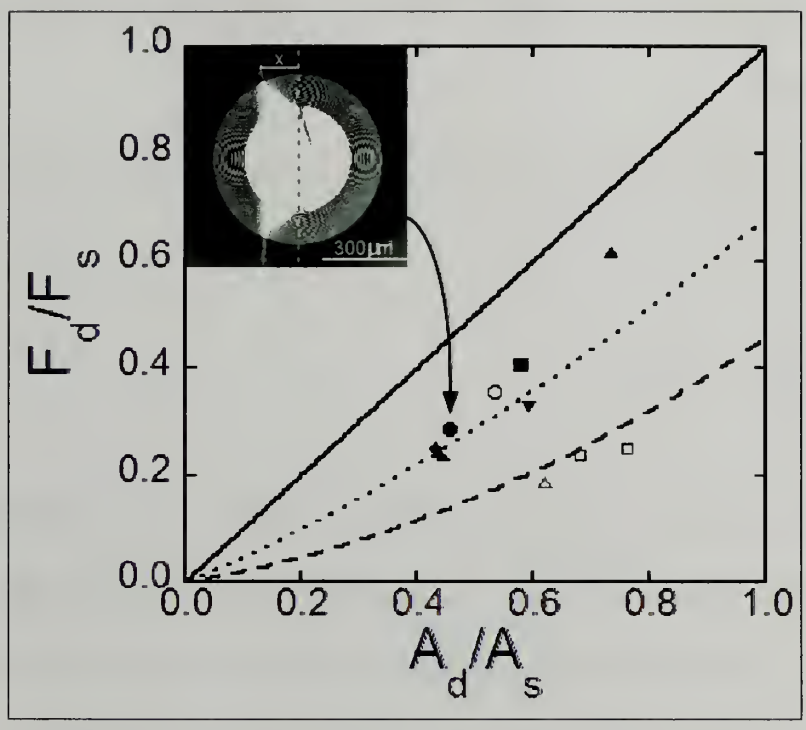

Figure 4.8: Frictional force at the defect (F_d) over the frictional force prior to any interaction with the defect (F_s) versus sliding contact area at the defect (A_d) over the sliding contact area prior to any interaction with the defect (A_s). (● - P=18mN, G~0.91MPa, h=1mm, ■ - P=18mN, G~0.51MPa, h=1mm, ▲- P=18mN, G~0.37MPa, h=1mm, ♦- P=19mN, G~0.95MPa, h=1mm, ▼- P=30mN, G~1.0MPa, h=1mm, ► - P=18mN, G~1.1MPa, h=0.4mm, ○ - P=40mN, G~1.00MPa, h=1mm, □ - P=30mN, G~1.00MPa, h=1.3mm, PDMS lens, and Δ - P=23mN, G~0.65MPa, h=1.3mm, PDMS lens) Inset shows how measurements of x/a and a_i/a_d were made.

on top of the initial contact area. As observed, these measured values adequately describe the observed force drop ratio for these experiments, independent of materials properties and normal force.

Based on these results, the lateral sliding force (F) for a general interface is described by:

$$F \propto \tau \left[\sum_{i=1}^{n} a_i \cdot f_{hi} \cdot f_{xi} \right]^2 \tag{4.12}$$

which accounts for the n contact areas each sliding under conditions of lateral confinement described by f_{hi} and f_{xi}. For a single contact, the relationship simplifies to $F = \tau A(f_h * f_x)^2$, which demonstrates that the effect of lateral constraint, f_h and f_x, must be accounted for in sliding contact problems to correctly predict the lateral force.

4.6 Summary

Defects, such as incisions, can provide a significant decrease in the sliding force for soft interfaces, as indicated by these results. The magnitude of this force drop is dictated by the defect's position within the sliding interfacial area, the materials properties, and the contact conditions. Building upon previous research on sliding friction, we can provide insight into the mechanism for this frictional decrease and how to take advantage of it for the design of interfaces. In the case of patterned soft surfaces correction factors including finite distance to a feature (f_x), contact splitting (Σa_i), and finite size effects (f_h) must be incorporated to fully describe the frictional changes associated with surface patterns. These correction factors become important for thin films, soft materials, and materials that have physical edges, such as topographically

patterned coatings. Overall, these results provide insight into the control of friction with topographically patterned surfaces, as well as fundamental insight into the relationship between sliding friction and interfacial area.

4.7 Acknowledgements

This work was supported by the National Scientific Foundation—Material Research Science & Engineering Center on polymers at The University of Massachusetts Amherst. We wish to thank Edwin Chan for his helpful discussions.

CHAPTER 5

FRICTIONAL RESPONSE OF WRINKLED SURFACES

5.1 Introduction

Topographic patterns have been shown to be very effective in the control, particularly the enhancement, of soft polymer adhesion[9, 20, 38, 47, 48]. This control in synthetic materials has largely been inspired by numerous examples in nature such as the gecko, the fly, and the spider. Although numerous mechanisms give rise to this control in adhesion, the topographic patterns play two important roles: 1) decreasing the stiffness of the surface allowing it to conform to rough surfaces 2) splitting the contact area which increases the contact perimeter. These mechanisms are effective for mode I loading of an interface, but how do topographic alter the friction of an interface? For smooth surfaces the friction in directly related to adhesion. For pattern surfaces, this enhancement of adhesion is coupled with loss of true contact area and changes in the tangential stiffness. We evaluated the role of patterns in friction by building upon results from our research group involving the fabrication and adhesion of wrinkled surfaces. Wrinkles form when the expansion or relaxation of an elastomeric material is confined. Surface wrinkles provide a simple, quick, robust method for topologically patterning surfaces over large length scales.

Southern and Thomas were the first to publish on the phenomena of surface wrinkling [25]. Upon swelling a laterally confined elastomer they noticed surface wrinkling, this instability was theorized previously by Green and Zerna for highly strained surfaces under indentation [14]. Various methods for wrinkling have been discovered since Southern and Thomas discovery, offering a variety of methods to

produce surface wrinkles. Tanaka *et al* showed that wrinkles formed upon swelling polymer gels and that the wrinkling could be manipulated through confinement and swelling agents [16, 49]. Figure 5.1 shows Tanaka's observations on wrinkling of a confined polymer gel submersed in water.

Another way to create a wrinkled surface is by applying uniaxial strain to an elastomer with a thin layer of a rigid material on top of it, which has been used to measure the modulus of the upper thin-film rigid material[23, 24]. This method is referred to as strain-induced elastic buckling instability for mechanical measurements (SIEBIMM). Tension in the stretching direction produces compression in the transverse direction. An elastic mismatch leads to a buckling instability at the surface creating aligned surface wrinkles. This method provides aligned surface wrinkles, whose periodicity can be tuned by the modulus mismatch of the elastic substrate and the thin film by the following equation (5.1).

$$d = 2\pi h\left[\frac{(1-\nu_s^{\,2})E_f}{3(1-\nu_f^{\,2})E_s}\right]^{1/3} \tag{5.1}$$

Where d is the wavelength of the buckles, h is the films thickness, ν is Poisson's ratio, and E is the elastic modulus. The subscripts f and s are indicative of the respective properties for the film and substrate. Images from the work of Stafford *et al* showing the changes in buckle periodicity with changing film thickness are shown in figure 5.2.

The adhesion of randomly wrinkled surfaces has been studied by Chan and Crosby[50]. They created wrinkle surfaces using a photocurable n-butyl acrylate (nBA) to create an elastomeric poly(n-butyl acrylate) (PnBA) substrate. This PnBA substrate is

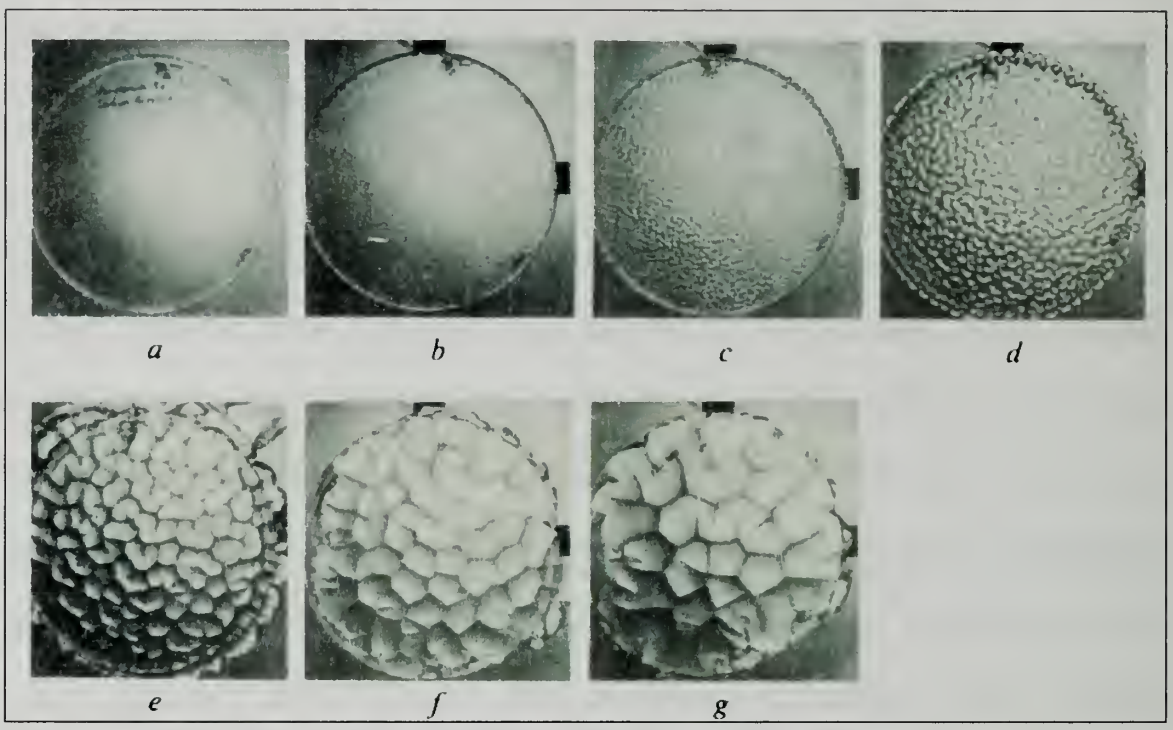

Figure 5.1: Evolution swelling an ionized acrylamide gel with water. Reproduced from Tanaka *et al.*[16]

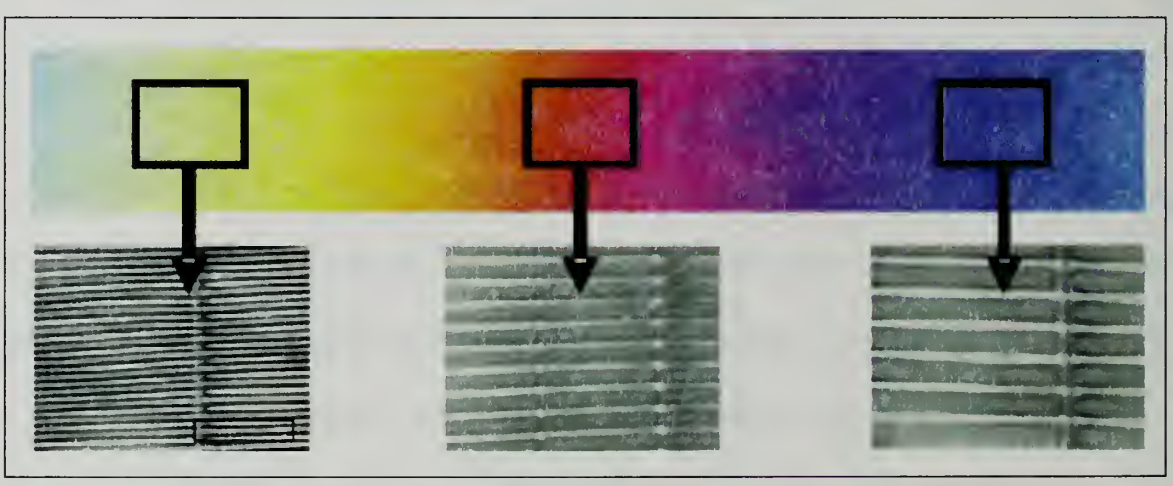

Figure 5.2: PS on silicon wafer (optical micrograph) and the corresponding buckled PS film on PDMS. (scale box, bottom left image is 50 μm) Reproduced from Stafford *et al.*[24]

then confined and swollen with nBA and cured again. These wrinkles are similar to the osmotically driven wrinkles first observed by Southern and Thomas[25]. Through a replication process they eliminate the effects of sample thickness and swelling, so that the effects of the wrinkles can be quantified. The results of there contact adhesion test are shown in figure 5.3. The results show an inverse scaling with wavelength and enhancements over smooth surfaces as the wavelength of wrinkles decreases. They attribute enhancements to an increase in the fracture length. Rather than one crack being driven to separate a smooth surface, multiple cracks are driven to separate each individual wrinkle and the total length is great than that of a smooth surface. As the wrinkle wavelength increases, the features act as surface roughness, decreasing the adhesion. They describe a critical wavelength that determines if the wrinkles enhance or decrease adhesion, which depends on the contact geometry (radius of the probe) and the materials properties of the interface (i.e. $\mathcal{G}_c$ an E*).

Work by Heuberger and coworkers on the friction of polymeric surfaces indicated that frictional force (F) was related to the adhesion energy by the following equation:

$$F = \frac{A(W_{eff} - W_0)\varepsilon}{2\sigma} \qquad (5.2)[51]$$

where W_{eff} is the effective surface energy, W_0 is equilibrium surface energy, A the contact area, σ is the characteristic dimension of the energy dissipation mechanism, and ε is the energy transfer efficiency per collision. This equation was intended for surfaces where the characteristic dimension or roughness was on the order of nanometers.

Theoretical work by Carbone *et al* evaluated the sliding of an elastomeric block on a wavy rigid surface[52]. They used the energy conservation principle to evaluate the frictional shear stress per control volume (see figure 5.4) by the following equation:

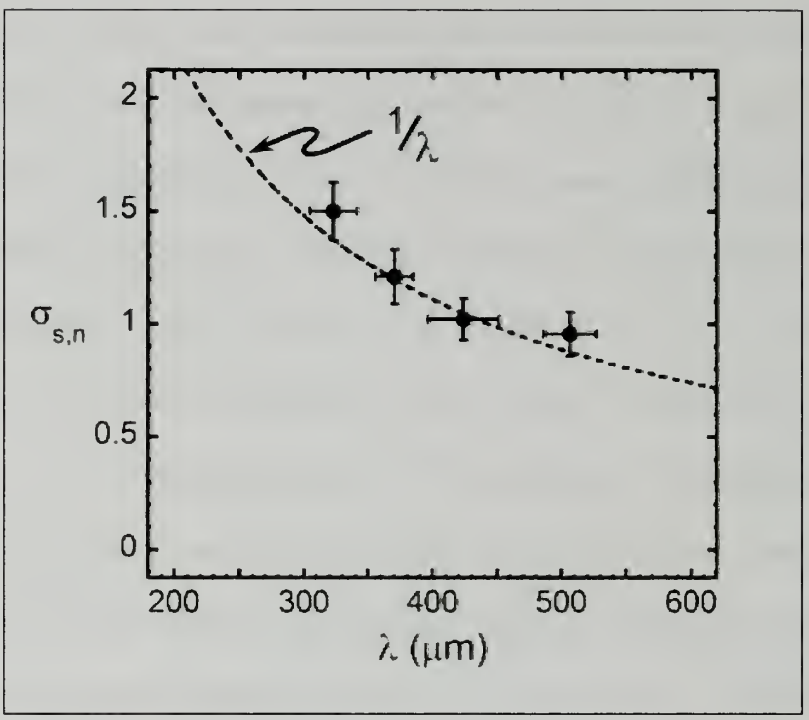

Figure 5.3: Separation stress comparison of the replicated wrinkled adhesives vs. the smooth, non-wrinkled analog as a function of λ. Reproduced from Chan *et al.*[50]

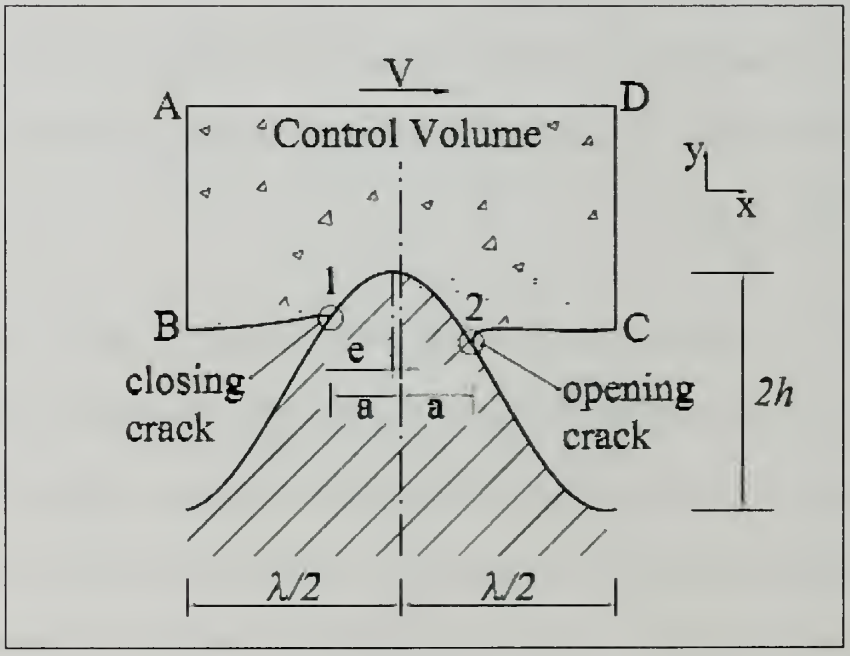

Figure 5.4 Schematic of a soft elastomeric block sliding over a single wave or wrinkle. Reproduced from Carbone *et al.*[52]

$$\sigma = \frac{G_2 - G_1}{\lambda} \quad , \qquad (5.3)[52]$$

where G_1 and G_2 are the strain energy release rates at the closing and opening cracks respectively and λ is the distance between wave peaks or the periodicity. The work by Carbone and coworkers is similar to that of Heuberger, the big difference is that Heubergers theory is used to describe features on the molecular length scale, while Carbone's theory is used to describe bulk sliding of an interface on a more macroscopic level.

While experimental work on the adhesion of wrinkled surfaces[50] along with theoretical work on friction[52] and adhesion[43, 52-55] of these surfaces has been completed, no research involving the experimental evaluation of wrinkled surfaces had been conducted. The theoretical work evaluated only sliding perpendicular to the wrinkles. It was therefore critical to understand how wrinkles influenced the sliding friction at a soft elastomeric surface. We evaluated this using a rigid lens sliding both parallel and perpendicular to aligned wrinkles on a soft elastomeric substrate (figure 5.5). Understanding this manipulation of friction through the use of surface wrinkles is critical not only to the fundamental understanding of patterned surfaces, but also to the development of high performance smart frictional surfaces that can be tailored to exact specifications.

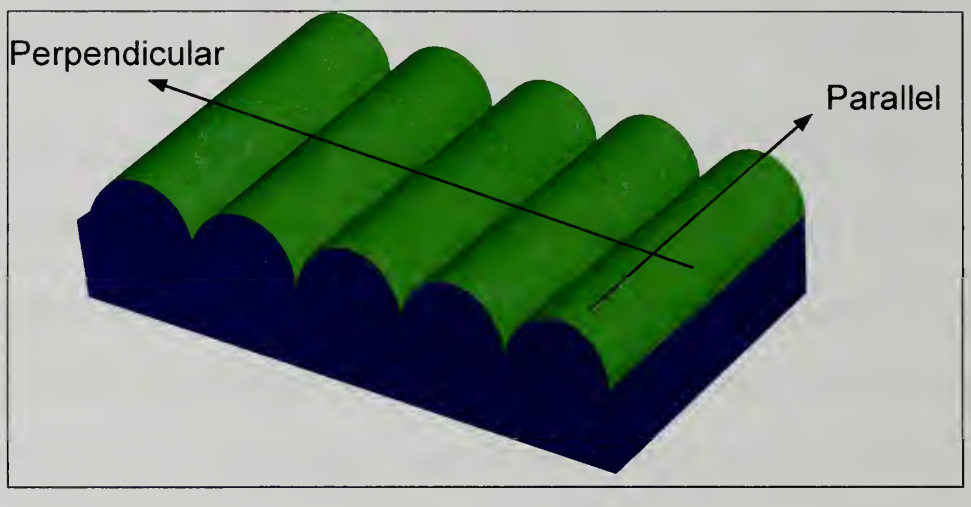

Figure 5.5: Cartoon schematic of the sliding directions of a wrinkled surface.

5.2 Experimental

Aligned wrinkles were used instead random wrinkles so that the effect of sliding both parallel and perpendicular could be deconvoluted and also because of the existing theory with regards to sliding perpendicular to wrinkled surfaces. The method of wrinkling the surface builds upon work by Efimenko *et al.*[22] Crosslinked polydimethylsiloxane (PDMS) (Dow Corning's Sylgard® 184) samples were prepared using three different crosslinker to prepolymer ratios 1 to 10, 1 to 15, and 1 to 20. Samples were cast as films 1mm thick and dog bone shaped specimens were cut from the films. The dog bones were then subjected to 30% uniaxially applied mechanical strain and exposed to ultraviolet light in the presence of ozone (UVO) for durations of 45, 60, 75, and 90 minutes converting the top layers of PDMS to a silica like layer [24]. Ultra-violet light in the presence of atmospheric oxygen was used to convert the surface of PDMS into a silica like layer[56]. Atmospheric oxygen was converted into ozone by 185 nm UV light, which was then converted into molecular oxygen by 254 nm UV light. The molecular oxygen cleaved the PDMS and created a thin layer of SiO_x (<100nm), where x is at most 1.5. CO2, water and volatile organics were removed during this process. This conversion is diffusion controlled and hence the "film" is a gradient starting with SiO_x and changing into PDMS as the depth increase, but can be modeled as an effective layer as shown by Chan *et al*[18].

To eliminate the convolution of surface chemistry, modulus changes in the upper layer, and residual stress, a replication of the wrinkles was created and used as a mold for the final PDMS testing samples. A UV curable optical adhesive (Norland Optical Adhesive 60, purchased from Edmund Optics) allowed for the inverse replication of the

wrinkled surface into a rigid material. This cast was then used to form aligned wrinkled surfaces of PDMS that were not subjected to compression or tension, thus the final sample contained aligned wrinkles with uniform surface chemistry and bulk modulus. Samples of one crosslinker to prepolymer ratio (1 to 10) were made from the molds for each amplitude-wavelength combination. The wrinkled PDMS surfaces were then swollen in hexane for two days and dried to minimize the number of free siloxane chains at the surface. The entire production of uniaxially aligned PDMS wrinkled surfaces is shown in figure 1. The entire wrinkle fabrication technique is shown in figure 5.6.

Chan *et al* has shown that varying the UVO exposure time changes the periodicity of the buckled surfaces created using a similar substrate exposed to osmotic stresses instead of uniaxial tension[18]. This control over the wavelength has been described by Harrison *et al*[23] in terms of modulus mismatch between PDMS and a thin film of polystyrene and thickness of the upper thin film. They also described how strain controlled the amplitude of the wrinkles produced in this manner. In this set of experiments the wavelength and amplitude were controlled by the crosslinker to prepolymer ratio of the substrate and also the UVO exposure time. All samples were characterized through microscope image for wavelength. The NOA molds were also characterized using profilometry in order to confirm periodicity and also acquire amplitude. A sample profilometry result is shown in figure 5.7.

The aligned wrinkles were then subjected to frictional experiments using the custom built setup shown in figure 3.1. A polished fused silica glass hemisphere (R, radius of curvature, = 5mm) was translated in contact with the wrinkles both parallel and perpendicular to the alignment. Sliding experiments were also conducted on a flat PDMS

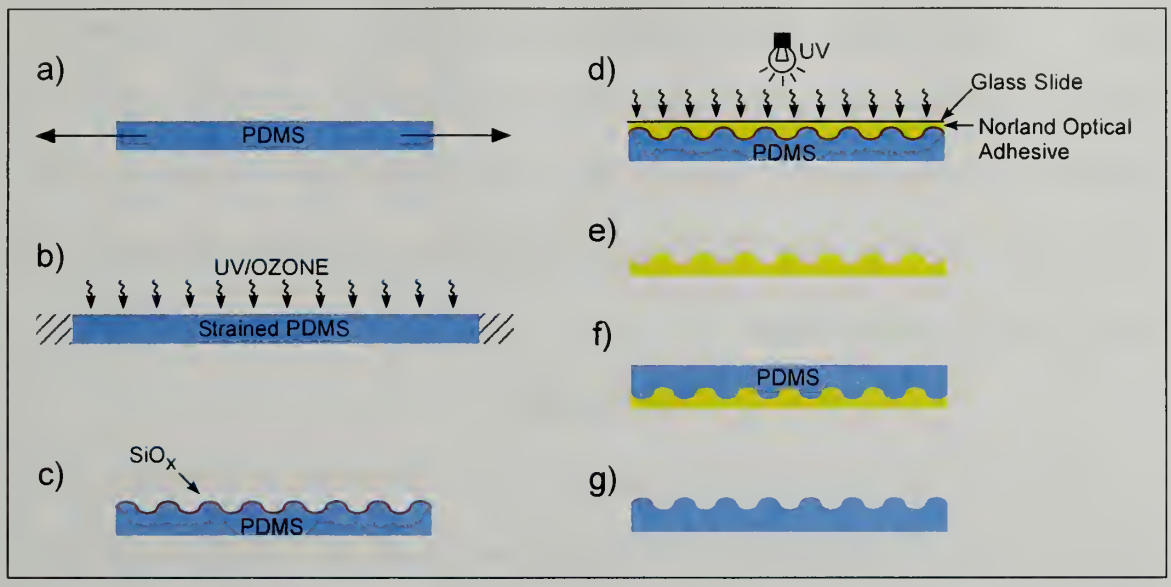

Figure 5.6: Fabrication of aligned wrinkles surfaces. a) PDMS substrate is subjected to 30% uniaxial strain b) The strained PDMS is exposed to ultraviolet light in the presence of ozone c) The PDMS substrate is released creating aligned wrinkles at the surface d) The wrinkles are covered with Norland Optical Adhesive (NOA) and exposed to UV light e) The cured NOA mold is removed from the wrinkled surface creating an inverse replica f) PDMS is molded of the NOA replica g) The NOA is removed leaving unstressed PDMS aligned wrinkles of the same modulus and surface chemistry.

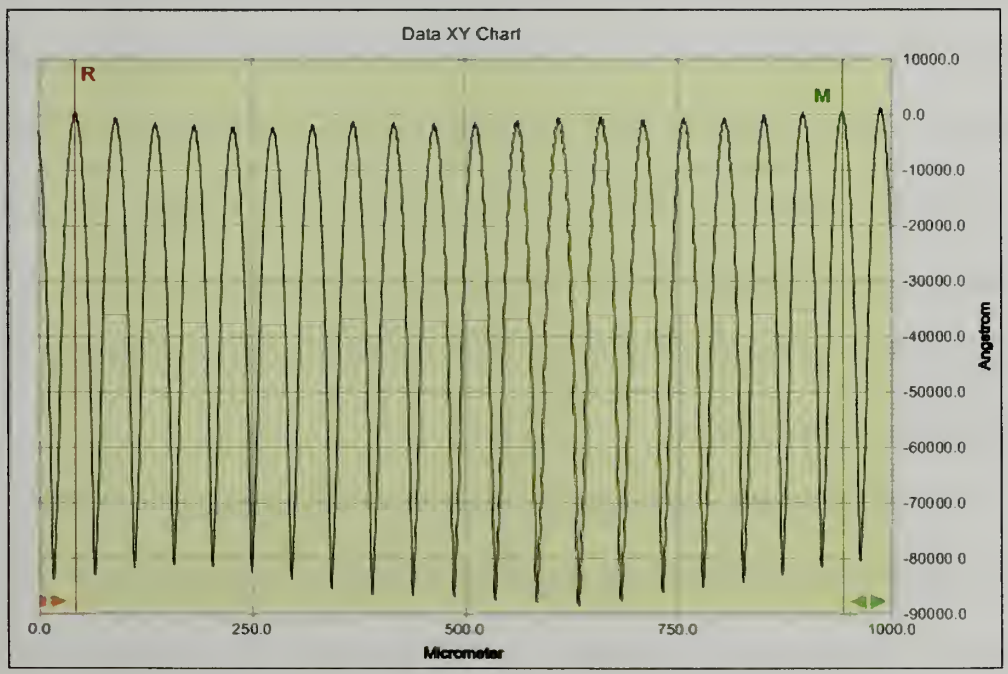

Figure 5.7: Example of the profilometry results of the wrinkled surfaces showing the regularity of the surface features.

surface as a control. Lateral sliding force, sliding distance, and images of the interfacial area were recorded while applying a constant normal force (P~23mN) for all experiments excluding the load dependence study. On one of the wrinkled surfaces, loads of 10, 30, 60, 80, and 110 mN were applied sliding in both directions. The lateral velocity (v) was fixed at 5μm/s for all experiments.

5.3 Results

Representative data showing the sliding force as a function of sliding position is shown in figure 5.8. Oscillations in the sliding force for the flat sample are associated with the formation and attachment of Schallamach waves [30, 57]. In the wrinkled sample, sliding both parallel and perpendicular to the wrinkles, the frictional force does not oscillate, maintaining a constant value, which is associated with a true-sliding frictional mechanism. It should be noted that from the sliding images of the wrinkled surface, the critical load required to collapse the wrinkles was not reached and hence the valleys of the wrinkles were not in contact with the slider[43]. The critical normal load per surface area for collapsing surface wrinkles under non-sliding conditions scales with the wrinkle amplitude, modulus of the wrinkles and inversely as the buckle periodicity[58]. Sliding parallel to the wrinkles provided a decrease in the sliding frictional force compared to the flat surface, and the decrease was greater for sliding perpendicular to the wrinkles.

A load dependence study was conducted on the sample with an aspect ratio of 0.135. Frictional experiments were run sliding parallel and perpendicular to the wrinkles and also on a flat surface for all loads evaluated. The results are shown in figure 5.9.

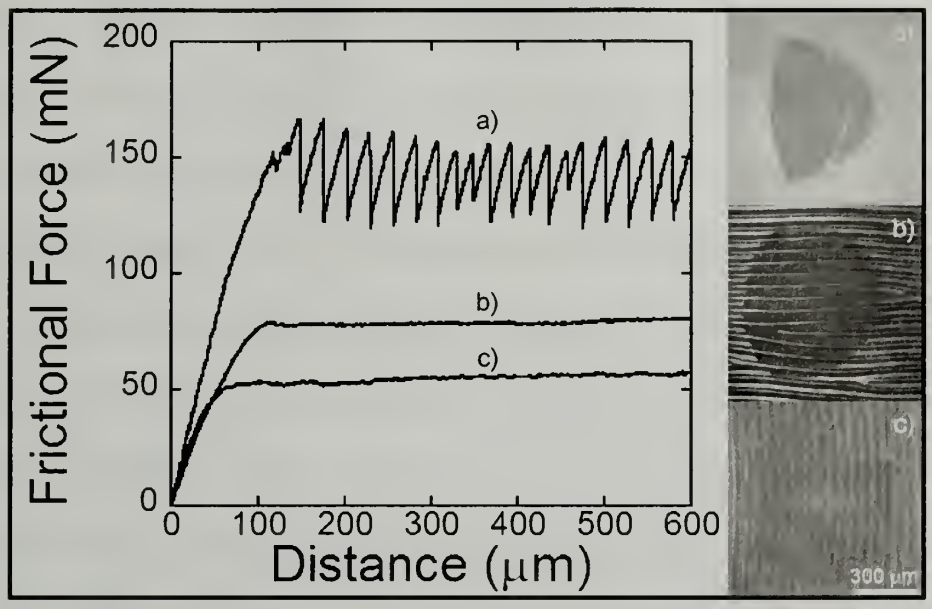

Figure 5.8: Representative force-displacement curves and sliding images for flat (a) and wrinkled surfaces (b,c).

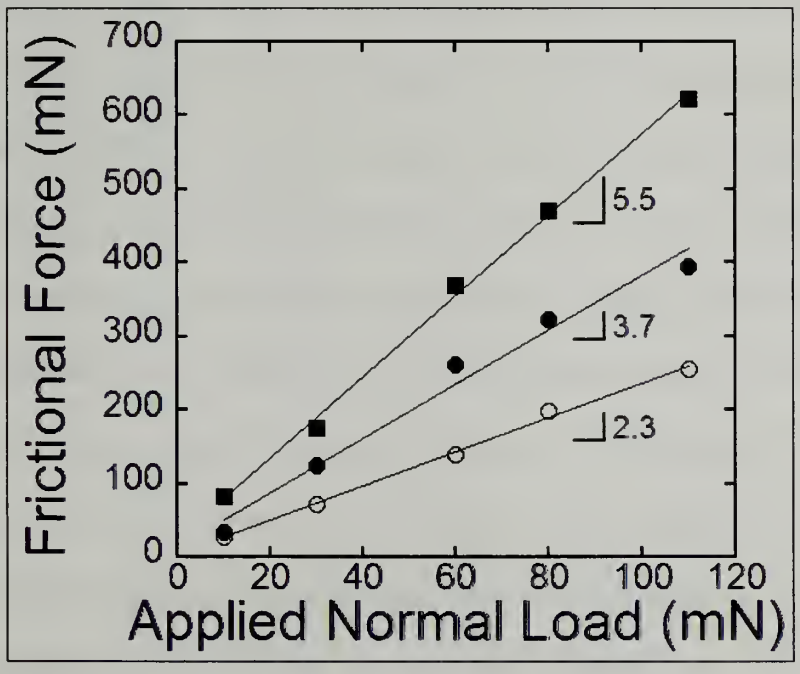

Figure 5.9: Frictional force versus normal load. (■ - flat surface ● – sliding parallel to the wrinkles ○ - sliding perpendicular to the wrinkles)

Figure 5.9 shows clearly that three different coefficients of friction were required to describe these surfaces, although the interfacial chemistry/composition is identical for each data set. At a load of 60 mN, sliding parallel to the wrinkles, portions of the wrinkled surface were collapsed during sliding; however this change did not appear to drastically change the relation between frictional force and applied normal load.

Using the procedure outlined above, we produced a library of surface-wrinkled samples with different aspect ratios, or h/λ, as shown in figure 5.10. Figure 5.10 shows that the amplitude increased linearly with the buckle periodicity of the wrinkles. The linear relationship of amplitude to buckle periodicity at a constant compressive strain has been described previously in scaling by Cerda and Mahadevan[59].

The frictional force of the wrinkled surfaces sliding parallel and perpendicular to the wrinkle alignment direction was normalized by the frictional force for a flat PDMS surface and plotted versus aspect ratio (figure 5.11) as well as changes in the normalized contact area (figures 5.12, 5.13). Figure 5.11 indicate the frictional force does not change much with aspect ratio sliding parallel to the wrinkles, while it appears to be dependent on the aspect ratio sliding perpendicular to the wrinkles. These results show in figures 5.12 and 5.13 indicate that in both sliding directions, changes in contact area alone can not describe the changes in friction. Figure 5.14 re-plots this data in terms of normalized shear stress versus aspect ratio. From this plot its appears that sliding perpendicular to the wrinkles the shear stress scales inversely as the aspect ratio, while sliding parallel to the wrinkles the normalized shear stress seems to level off at around 0.6.

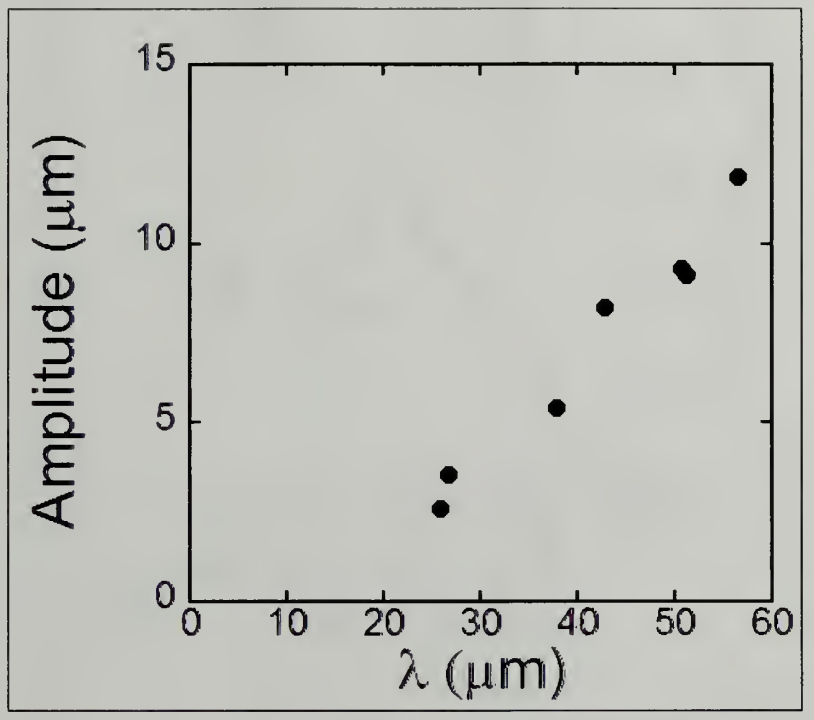

Figure 5.10: Amplitude versus buckle periodicity (λ).

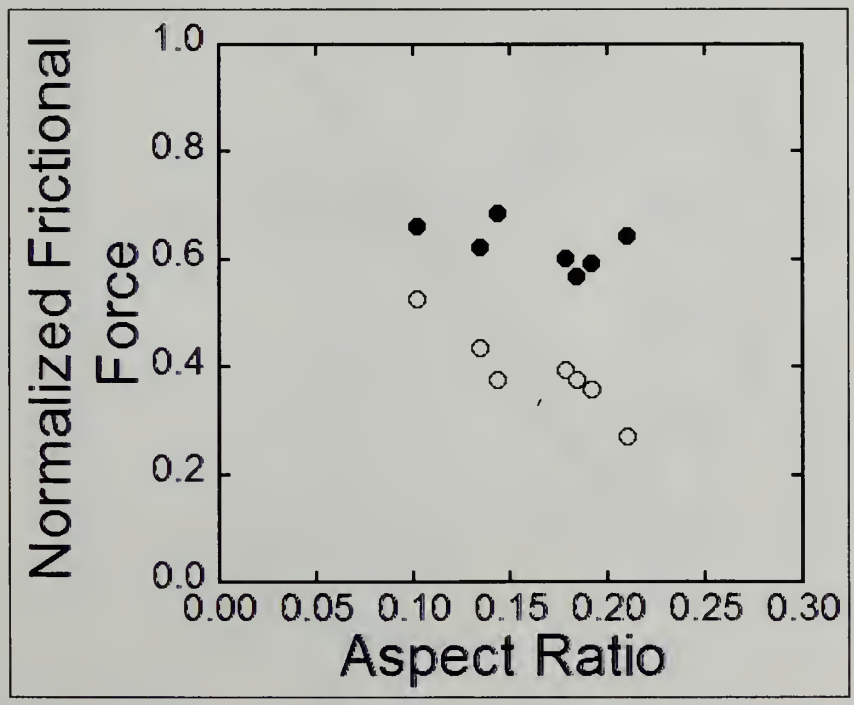

Figure 5.11: Normalized frictional force versus aspect ratio. (● - sliding perpendicular, ○ – sliding parallel)

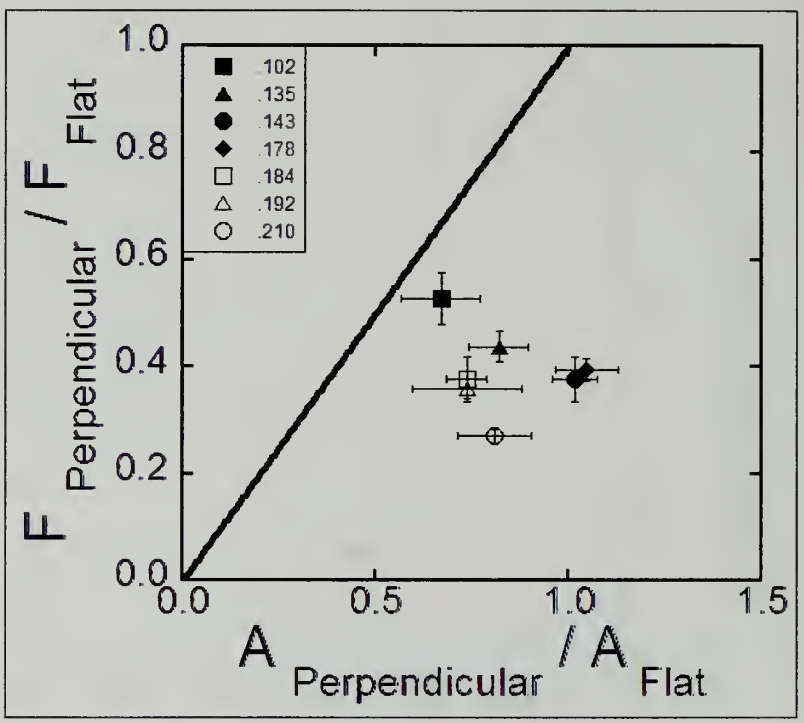

Figure 5.12: Normalized frictional force versus normalized contact area sliding perpendicular to the wrinkles. (Key indicates aspect ratio)

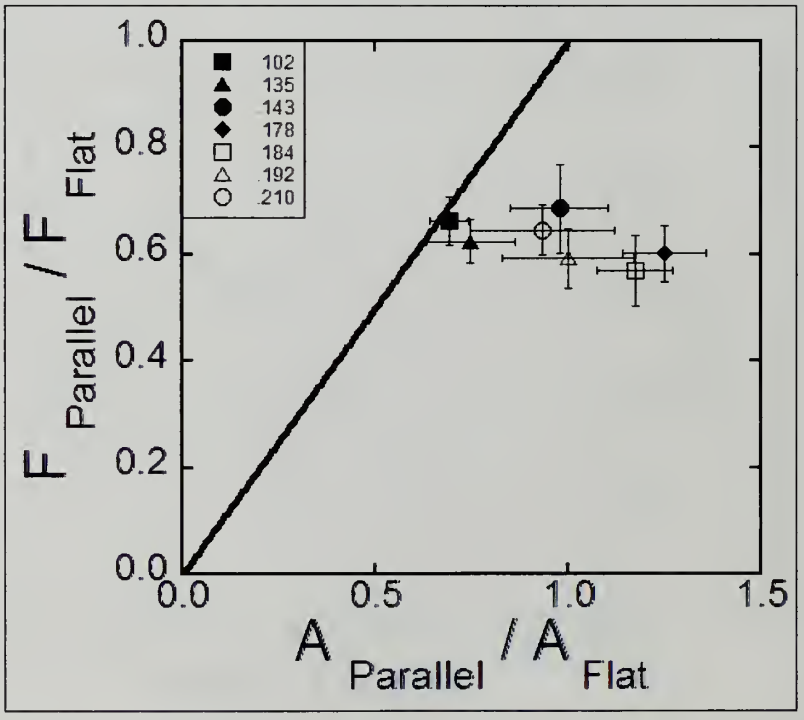

Figure 5.13: Normalized frictional force versus normalized contact area sliding parallel to the wrinkles. (Key indicates aspect ratio)

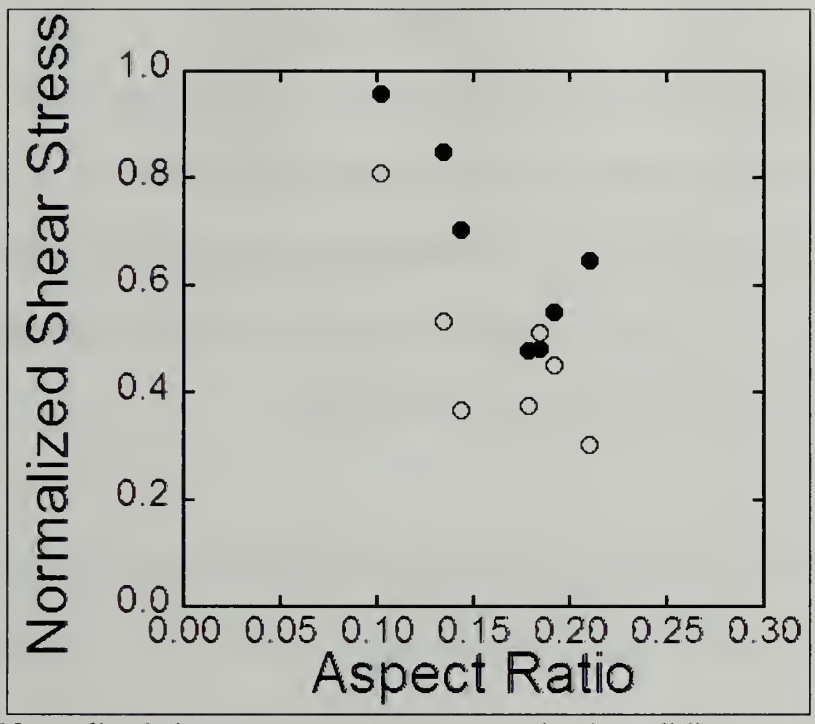

Figure 5.14: Normalized shear stress versus aspect ratio. (● - sliding perpendicular, ○ – sliding parallel)

5.4 Discussion

To understand the change in frictional force associated with surface wrinkles, we used a classical friction model presented by Bowden and Tabor, $F = \tau * A$ [1], where F is the measured frictional force, τ is the interfacial shear strength, and A is the true contact area. In chapter 4, we adapted this model to account for changes in tangential stiffness through the use of a non-dimensional correction factor f_x:

$$F = \tau * A * f_x^{\,2}. \tag{5.4}$$

The interfacial shear strength can be related to critical energy release rate for propagating the interfacial fracture at the slider/substrate interface ($\mathcal{G}_c$) using the following relationship:

$$\tau \propto \frac{\mathcal{G}_c}{\ell}, \tag{5.5}$$

where ℓ is a materials-defined length scale associated with the fracture process at the slider/substrate interface. Substituting back into equation 5.4 we have a general scaling for frictional force:

$$F \propto \frac{\mathcal{G}_c A f_x^{\,2}}{\ell} \tag{5.6}$$

According, to Hertzian mechanics, the contact area, A, between a rigid slider and flat substrate should scale with $P^{2/3}$. Using this relation, Barquins and Roberts modified Bowden and Tabors' scaling to relate the coefficient of friction to applied normal load and radius of curvature[29], but their testing of the normal load scaling was limited. For our experiments, over the range of normal loads measured, we measured $A \propto P$. (Figure 5.15) Therefore, we can replace area with load as follows:

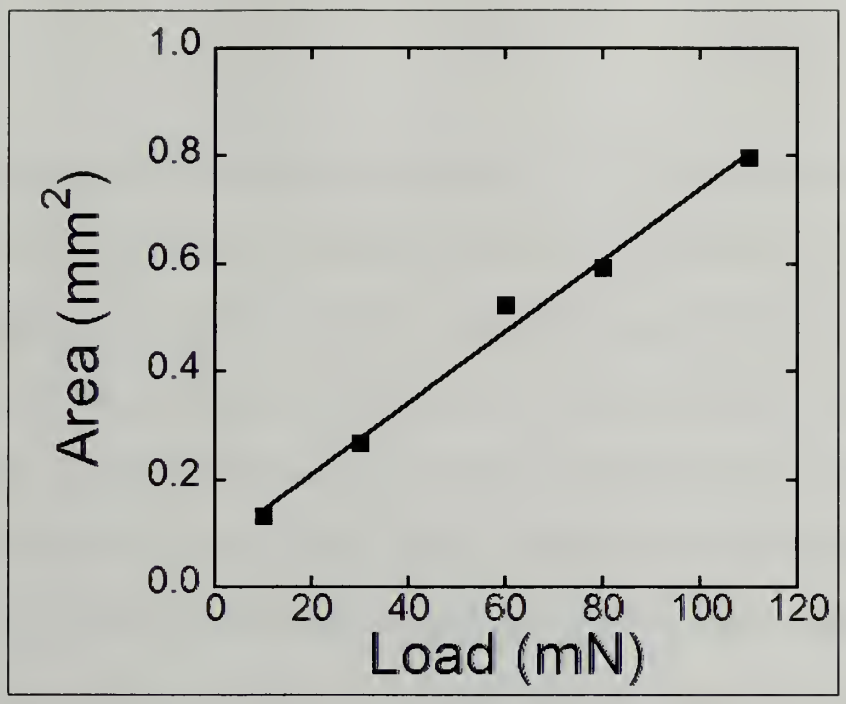

Figure 5.15: Sliding contact area versus normal load (flat surface).

$$F \propto \left(\frac{\mathcal{G}_c f_x^{\,2}}{\ell} \right) P. \tag{5.7}$$

This relationship supports the linear scaling between frictional force and normal load in Figure 5.9 and indicated that the tangential stiffness correction factor, f_x, and $\mathcal{G}_c$ were primarily responsible for the different slopes of Figure 5.9 for each of the samples.

For both wrinkled samples, f_x was measured to be approximately 0.72; therefore, accounting for the decreased slopes relative to the non-wrinkled samples. Furthermore, sliding perpendicular to the wrinkles caused a change in the fracture angle at the slider/substrate interface during sliding. Similar to the effect of changing the angle of peel in a peel test, the change in the fracture angle altered the critical value of $\mathcal{G}_c$ for propagating a fracture, allowing sliding to proceed[60]. For true sliding, the fracture angle would be 0°, or mode II fracture. For sliding with Schallamach waves, fracture proceeds at angles near 90° or mode I, associated with the lowest $\mathcal{G}_c$[61]. For the wrinkled surfaces, Schallamach waves were not observed when sliding perpendicular to the wrinkle alignment direction since the wrinkle periodicities were similar to the Schallamach wave periodicities measured in the flat sample. We hypothesize that the surface wrinkles serve the same role as Schallamach waves in altering, i.e. lowering, the $\mathcal{G}_c$ for lateral displacement of the interface. Furthermore, we hypothesize that the aspect ratio of the surface wrinkles alters the local fracture angle, i.e. fracture mode, thus leading to the decrease in friction as the aspect ratio increased (figure 5.11).

5.5 Summary

We have shown that surface wrinkles can reduce the sliding frictional force of a sliding hemispherical lens. Three separate coefficients of friction were required to

describe sliding parallel, perpendicular, and on a flat surface, even though these interfaces are comprised of identical materials. The change in frictional force can not be described solely from changes in contact area, indicating that the wrinkles are not acting as ordered roughness on the surface. Rather, changes in tangential compliance and interfacial fracture angle, or mode, are responsible for the altered frictional mechanisms. These control factors should apply to both anisotropic and isotropic surfaces, as well as other topographic surfaces, thus giving guidance in the design of smart surfaces that can be tuned to the desired frictional and adhesional properties.

5.6 Acknowledgements

This work is supported by the National Scientific Foundation – Material Research Science & Engineering Center on polymers at The University of Massachusetts Amherst.

CHAPTER 6

ALIGNMENT OF SURFACE WRINKLES USING SURFACE DEFECTS

6.1 Introduction

In the previous chapters we have evaluated the effects of naturally occurring and induced features at the surface of a soft elastomer. In this chapter we propose a simple, robust method to incorporate the aligned wrinkles of chapter 5 and the defects presented in chapter 4 to an elastomeric surface with a thin rigid coating. This hierarchical structure provides an interesting surface that can be described frictionally from the previously presented research. This work was done in collaboration with three grade school teachers as part of the NSF-MRSEC sponsored Research Experience for Teachers program. Their hard work and dedication helped develop the robust method of aligning surfaces wrinkles presented in this chapter.

Wrinkled or buckled surfaces with well-defined wavelengths can be created by a variety of methods, which typically rely upon the deposition or attachment of a thin rigid film on an elastomeric substrate and subsequent compression of the film/elastomer composite beyond a critical strain. Mechanical compression[22], thermal mismatch strains[17, 62], and differential swelling[18] all have been demonstrated as viable routes for strain-induced wrinkling. Figure 6.1 shows examples of these three techniques. In the case of differential swelling, the film resists the swelling of the underlying elastomer, leading to the development of a compressive stress near the film/elastomer interface. Experimentally, the general phenomena of swelling-induced wrinkling was first seen by Southern and Thomas who evaluated the swelling of a laterally confined rubber block with various swelling agents.[25] Subsequently, several research groups have extended

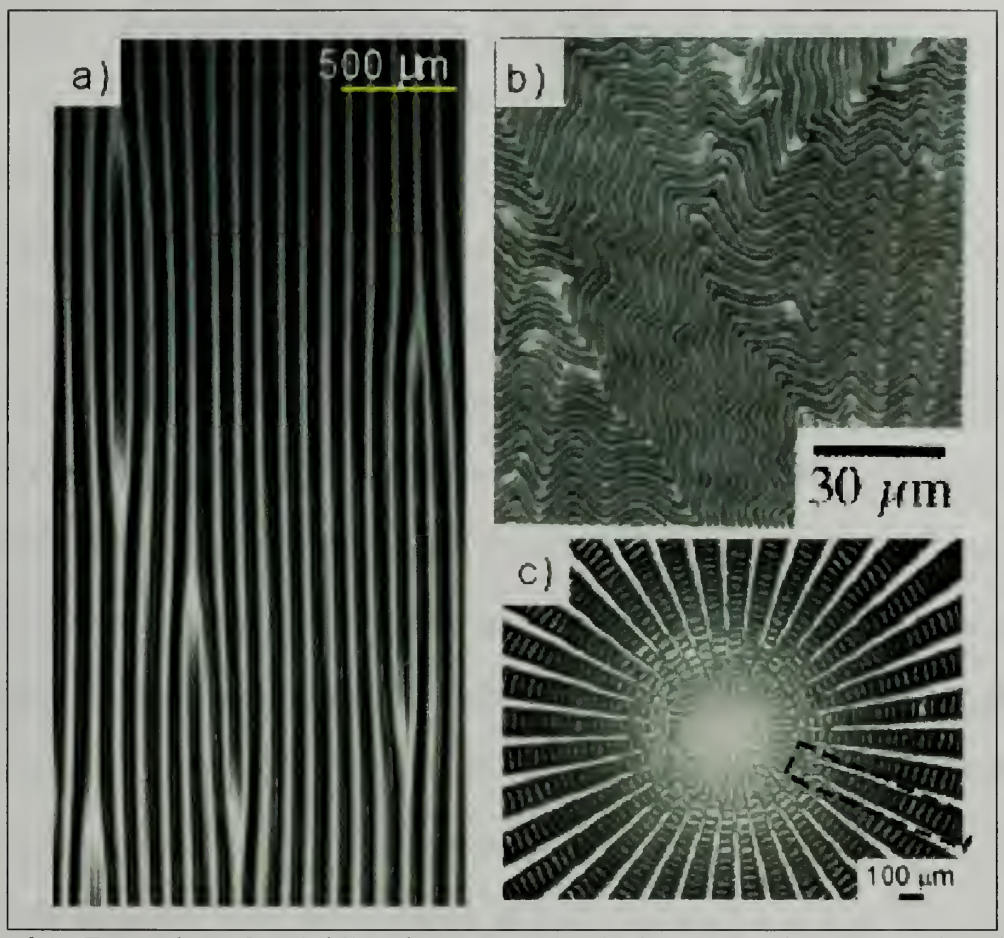

Figure 6.1: Examples of wrinkling by (a) mechanical compression (Reproduced from Efimenko et al[22]), (b) thermal mismatch strains (Reproduced from Bowden et al[63]) , and (c) differential swelling (Reproduced from Chan et al[18]).

this process by imposing constraint through a surface attached film, which is especially attractive for the scaleable fabrication of 'smart' or responsive coatings.

Under ideal conditions, surface wrinkling from equi-biaxial stresses, such as swelling or thermal stresses, results in a herringbone pattern as described by Chen and Hutchinson[21]. Although herringbone patterns are sufficient or convenient for the topographic control of certain surface properties, such as adhesion, many potential applications of wrinkled surfaces will require the long-range control of non-herringbone wrinkle arrangements. Previous research has largely relied upon lithographic methods to locally alter the equi-biaxial stress state, thus altering the wrinkling morphology. For example, Bowden and co-workers[17] used a topographically patterned elastomer to align wrinkles local to the topographic edges. Chan and Crosby (figure 6.1(c)) demonstrated the use of lithographically patterned constraining films, in absence of topographical changes, to produce aligned wrinkled surfaces for osmotically-driven wrinkles. In both of these methods, the applied equi-biaxial stress on the rigid upper layer changes locally to a primary compression parallel to an edge discontinuity, resulting in the alignment of wrinkles. Although both methods are powerful, they ultimately rely upon top-down processing methods, which can be potentially limiting for laterally extensive applications. In this chapter, we similarly used stress discontinuities to locally alter the equi-biaxial structures of osmotically-driven wrinkles, but our process does not rely upon lithographic processing. Instead, a simple process of fracturing the upper layer through the use of controlled uniaxial strain is used. This process not only leads to local rearrangement, but demonstrated long-range order across samples with lateral dimensions on the order of centimeters. The combination of osmotically-driven surface wrinkles and

non-lithographic routes to long-range alignment makes this process especially attractive for numerous applications.

6.2 Experimental

To create wrinkled surfaces, we used a crosslinked polydimethyl siloxane (PDMS) (Dow Corning's Sylgard® 184) as the elastomeric substrate. The crosslinked PDMS films were prepared by mixing 1 part crosslinker with 10 parts prepolymer. The uncured mixture was poured into a circular mold with a diameter of 50 mm and a depth of 1mm. The samples were then cured at 70° Celsius for 2 hours. The cured samples were cut with a dog bone shaped template to control the uni-axial strain distribution. The upper rigid layer was created by exposing the elastomeric substrate to ultra violet light in the presence of ozone (UVO). This UVO process converts the surface of the PDMS into a silica-like layer[56, 64, 65] (SiO_x). The dog bone samples were subjected to 15, 30, 45, or 60 minutes of ultraviolet/ozone exposure using Jelight's model number 342 UV/Ozone cleaner. The samples were then immersed in ethanol which swells PDMS. The rigid SiO_x layer restricts the swelling of the upper portion of the PDMS, while the lower portion is allowed to expand. Upon exceeding a critical osmotic stress which develops a compressive stress at the SiO_x/PDMS interface, the surface wrinkles. This stress (σ_c) for bucking a thin film on elastic substrate is:

$$\sigma_c = \frac{E_f}{4(1-\upsilon_f{}^2)}\left(3\frac{E_s(1-\upsilon_f{}^2)}{E_f(1-\upsilon_s{}^2)}\right)^{2/3} \qquad (6.1)[66]$$

where E_f and E_s are the elastic modulus of the film and the substrate, and ν_f and ν_s are the Poisson's ratio of the film and substrate, respectively. Figure 6.2(a) shows the wrinkling

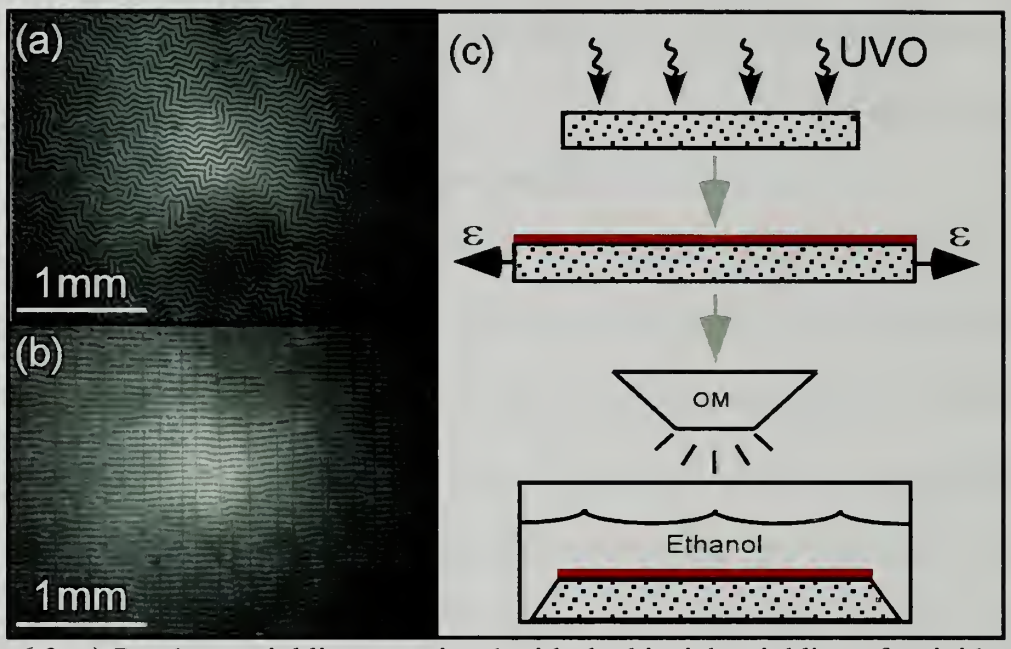

Figure 6.2: a) Random wrinkling associated with the biaxial wrinkling of a rigid surface on a soft elastomeric surface b) Aligned wrinkles created through the use of surface defects c) Wrinkling process. Reproduced from Rand et al[67].

of a defect or pattern free surface using this method. In this situation, wrinkle direction is random on the surface showing no noticeable order.

To align the surface wrinkles, we applied uni-axial strain to the substrate, after SiO_x formation, to provide discrete fracture lines in the SiO_x layer. After release of the uniaxial strain, subsequent swelling of the substrate in ethanol provided aligned wrinkles perpendicular to the fracture direction. An example of these aligned wrinkles is shown in figure 6.2(b) and the alignment process is summarized in figure 6.2(c). While the longevity of the wrinkle structure was not explored, these structures remained the same for 6 months while immersed in ethanol.

6.3 Results and Discussion

To evaluate wrinkle alignment using this fracture process, we varied the UVO exposure time and applied uniaxial strain. The UVO exposure time determines the conversion of the upper most layer to SiO_x, changing the thickness (h) and modulus of this rigid upper layer (E_f).[65] Both h and E_f control the wavelength (λ) of the surface wrinkles:

$$\lambda = 2\pi h_f \cdot \left(\frac{1}{4(1-\nu_f{}^2)} \frac{E_f}{E_s} \right)^{1/3}, \qquad (6.2)[66]$$

where Es is the elastic modulus of the PDMS substrate and ν_f is the Poisson's ratio of the SiO_x layer. For our material, similar to Chan and Crosby[18], we used a multilayer model for h_f and E_f to properly relate λ to the materials properties (Fig. 6.3).

For a wrinkled surface created using biaxial stresses, the length over which a wrinkle is ordered or aligned is referred to as the persistence length (ζ). The persistence length is,

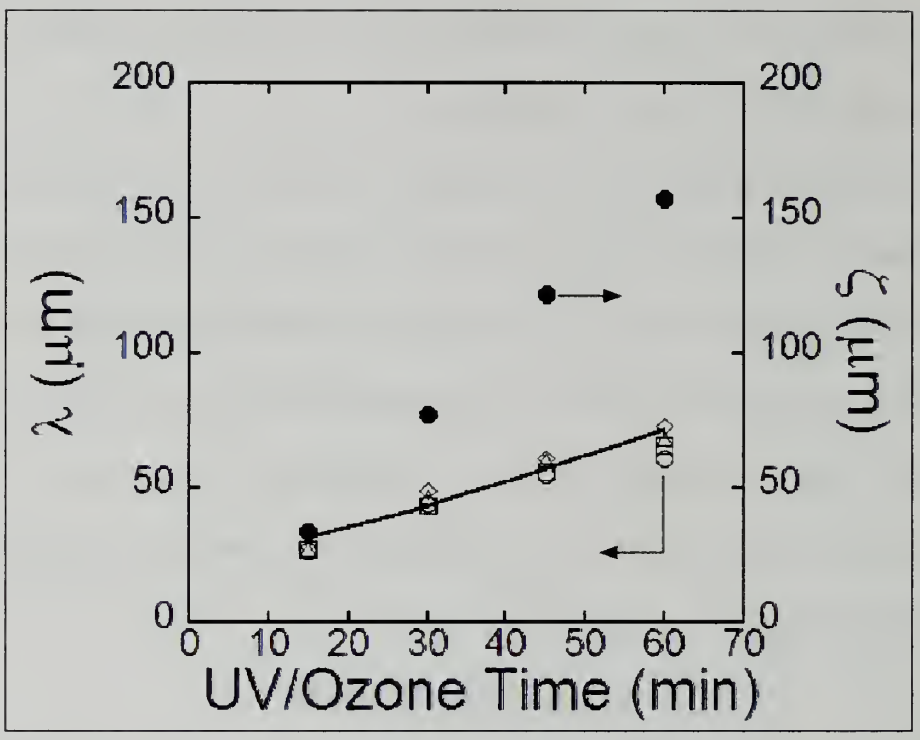

Figure 6.3: Buckle periodicity (λ) (open symbols) and characteristic distance (ζ) (closed symbols) versus UVO exposure time. (○– 0% strain, □- 10% strain, Δ-25% strain, and ◊-50% strain)

$$\zeta \approx \lambda\left(\frac{1}{2\Sigma^{1/2}} + 2\cdot\left(\frac{1}{4(1-\nu_f{}^2)}\frac{E_f}{E_s}\right)^{1/3}\right) \qquad (6.3)[19]$$

where Σ is not the strain applied prior to swelling, but rather the strain applied to the rigid upper layer from the osmotic stress developed from swelling. It should be noted that persistence length scales directly with wrinkle periodicity and hence increasing the wrinkle periodicity by increasing UVO exposure time thus increases ζ (figure 6.3). The persistence length as a function of UVO exposure time is shown in figure 6.3.

In Figure 6.3 all samples including samples with fractures are characterized in terms of the wrinkle periodicity. From the plot it is evident that this fracture process does not influence the wrinkle periodicity over the range of applied strains we evaluated. The characteristic distance was only measured for samples with 0% applied strain. Both measurements were made using the program Image J. Images of the various wrinkled surfaces were captured through the use of a microscope while the samples were still immersed in ethanol. Multiple images and measurements were used for the data shown in Figure 6.3.

The other variable, applied strain, controls the fracture process by dictating the average spacing between fracture lines <L>:

$$\langle L \rangle = c\varepsilon^{-\kappa} \qquad (3)\ [68]$$

where c is a constant, κ is an empirically-determined exponent, and ε is the applied uniaxial strain. The fracture spacing versus the applied strain is shown in figure 6.4 for various UVO times. Heinrich and co-workers indicated that κ changes at a critical strain (ε_c) and critical fracture spacing (L_c)[68]. Below ε_c, κ is equal to the Weibull exponent of the strength distribution of the film[68]. Fracture spacing versus strain is plotted in figure

6.4. At low strains the spacing is difficult to control uniformly, as noted in the error bars, but the spacings become more homogenous at higher strains.

Similar to previous work on wrinkle patterning[17, 18], in our process the stress discontinuity at the fracture causes a primary compressive stress to develop parallel to the fracture line. Therefore, upon exceeding a critical stress, surface wrinkles align perpendicular to a fracture line. This alignment persists for distances up to ξ away from the defect. Accordingly, if the average spacing between defects is smaller than ξ the wrinkles align across the entire surface. It should be noted that homogenous fracture spacing is not required for alignment as long as the fracture spacing is less than the persistence length of the wrinkles.

A phase map confirming the balance of oxidation time and fracture strain, i.e. persistence length and fracture spacing, is shown in figure 6.5. For all samples, a finite conversion of the upper layer to SiO_x must be achieved in order to fracture the SiO_x surface layer prior to fracturing the entire PDMS sample. At low UVO times (as seen in the 15 minute UVO sample), the conversion of the silica-like layer is not sufficient to provide fractures when subjected to strains of up to 50%. For longer UVO times, a critical processing strain can produce fracture lines, but systematic alignment of the surface wrinkles requires the applied strain to produce fracture line spacings less than ζ. This condition is satisfied for UVO times and strains in region II; whereas fracture lines in region I only produced local alignment. Although alignment in region II is achieved on average, some regions are observed where local fracture spacing is greater than ζ. One example of this condition is in the sample exposed to 30 minutes of UVO followed by a

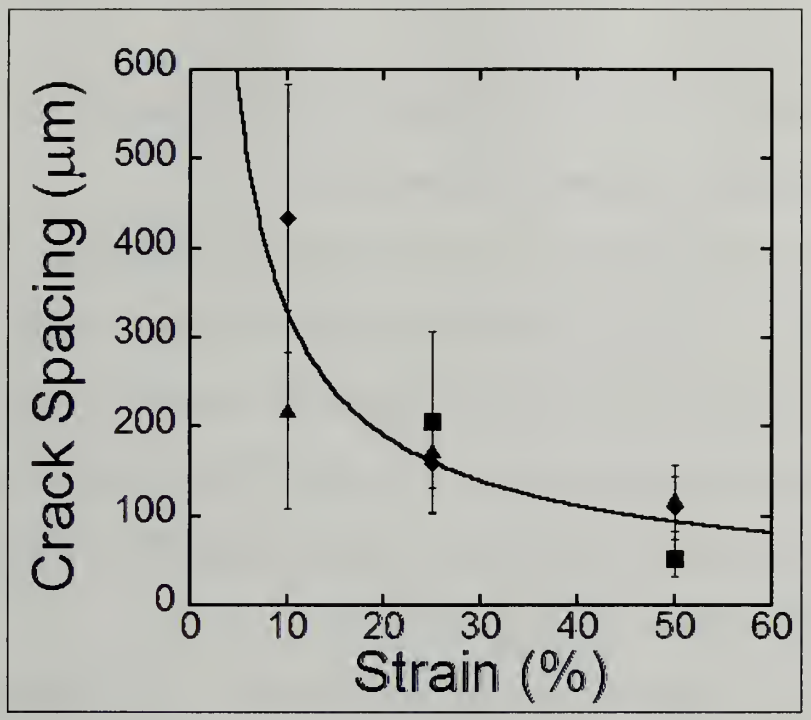

Figure 6.4: Crack or defect spacing versus applied uniaxial mechanical strain. (■- 30 minute UVO exposure, ▲-45 minute UVO exposure ♦-60 minute UVO exposure)

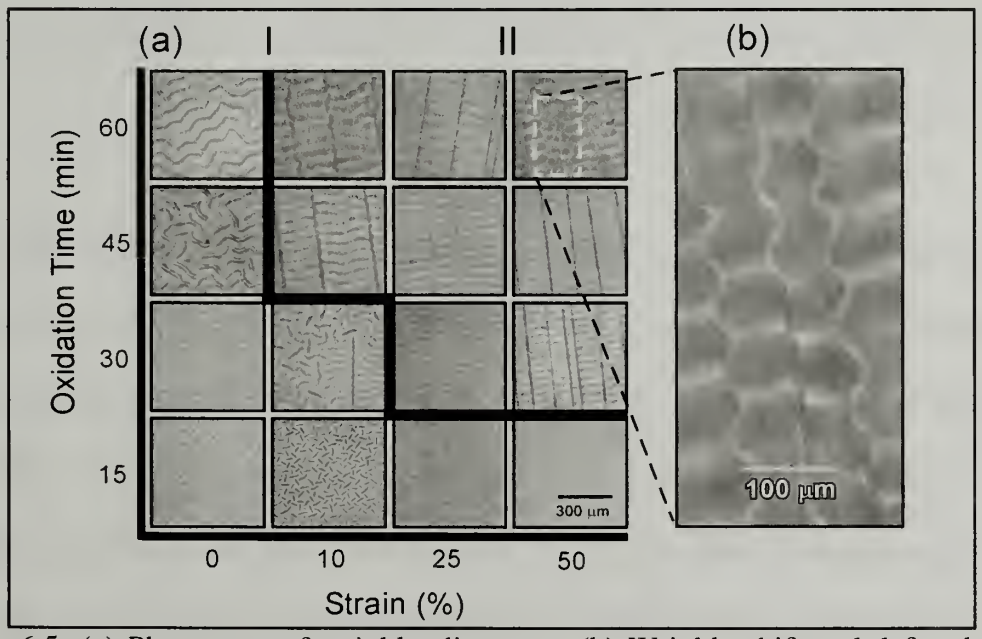

Figure 6.5: (a) Phase map of wrinkle alignment. (b) Wrinkle shift and defect buckling. Reproduced from Rand et al[67].

25% strain, the fracture spacing is much larger than ζ (~77μm), and hence biaxial strain causes the herring bone structure in the wider sections.

While smaller fracture spacings can be achieved at higher strains, it appears that these strains are not necessary to produce surfaces with aligned wrinkles, and perhaps may lead to misaligned regions as shown in figure 3(b), which is an enlarged portion of the wrinkles from the sample exposed to 60 minutes of UVO and subjected to 50% strain. In this high strain, high UVO time region, alignment of the surface wrinkles across the fracture line shifted as fracture spacing decreased.

We believe that the fracture depth increased in this regime, but this result has not been experimentally verified. Similar to work on stress transfer in the delamination test of thin films[69], an increased depth of the fracture line would minimize stress transfer between wrinkling regions. For shallow edge discontinuities, sufficient stress transfer leads to correlated wrinkling patterns across the defect.

6.4 Summary

In summary, we have developed a simple method to align osmotically-driven surface wrinkles over large length scales without the use of lithography. For this method, no template is required to orient the wrinkles. Uniaxial tension is used to define fracture lines with average spacings smaller than the persistence length. This process applies to elastic systems coated with a thin rigid material that undergoes fracture in uniaxial tension and wrinkles upon equi-biaxial compression above a critical stress. For equi-biaxial stresses induced by swelling, cross-linkable swelling agents can be used to "lock in" the wrinkle structures.[18] Such structures can be used as smart frictional and

adhesive surfaces, micro-fluidic devices, and other advanced applications as discussed in recent publications[9, 24, 70-72].

The work presented in chapters 4 and 5 should fully describe the frictional response of surfaces with wrinkles and fractures. The addition of fractures would provide a decrease in the frictional force sliding parallel to the wrinkle structures that would be caused by a decrease in the sliding contact area along with a reduction in the tangential area. Sliding perpendicular to the wrinkles the defects should not alter the frictional force dramatically, since the stresses trail off rapidly perpendicular to the sliding direction. These surfaces allow for the full tuning of the frictional response along with the ability to create anisotropy. Biaxial wrinkling of a rigid film on a soft elastomeric surface without defects proceeds by random isotropic wrinkles or in equi-biaxial a herringbone structure. Defects at large spacings can be used to add local order and at smaller spacing global alignment of the wrinkles. The spacing of the defects could be used to completely control the frictional anisotropy of these surfaces. The thickness of the film deposited on elastomer, the swelling agent, and the modulus of the elastomeric can all be used to tune the aspect ratio of the features, giving another way to tune the frictional response of these surfaces.

6.5 Acknowledgments

This work was supported by the National Scientific Foundation- Material Research Science & Engineering Center on polymers at The University of Massachusetts Amherst. We would like to thank Edwin Chan for his helpful discussions. We would also like to thank Greg Dabkowski, Renee Sweeney, Mary Morrissey, Lauren Hazel, and the NSF-MRSEC sponsored RET program at the University of Massachusetts.

CHAPTER 7

SUMMARY AND FUTURE WORK

7.1 Summary

This work has focused on the effects of patterns on soft polymeric friction. We started by looking at Schallamach waves, which are naturally occurring surface patterns that develop as a consequence of high adhesive forces at a soft sliding interface. After this we evaluate the influence of the simplest pattern, a single defect or feature, on the sliding force. The defect can be modeled as the edge of a single feature and the work presented on this can be translated to patterns with multiple features. In this work it was critical to understand the fundamentals of Schallamach waves prior to examining the effect of a defect, since they were present in most of the experiments. After looking at one feature, we moved on to evaluate a fully patterned surface of aligned features. We evaluated sliding parallel and perpendicular to the features and compared it to a flat substrate of the same modulus and surface chemistry. Finally, we developed a method to create aligned surface wrinkles at a soft elastomeric surface over large length scales without using lithography or selective oxidation. Alignment was created through the use of surface defects, the frictional effects of which had been explored as mentioned to model topographically patterned surfaces.

The work presented here has been conducted to evaluate the friction of patterned soft polymer interfaces. Any disruption in a smooth sliding surface can be considered a defect, so in essence we have conducted experiments using various defects at a sliding interface and also developed a new method to utilize defects in a surface for alignment of

surface wrinkles. This work lays the fundamental groundwork for the design of tunable sliding soft elastomeric surfaces.

7.1.1 Length Scales of Naturally Occurring Surface Patterns: Schallamach Waves

We conducted experiments to understand the fundamentals of Schallamach waves. The goal was to evaluate the natural length scale of Schallamach waves and relate that to the materials properties of the sling interface. The balance of interfacial and bulk contributions, as described by the material length scale $\mathcal{G}_c$ /E*, was related to the periodicity (λ) of Schallamach waves. This deconvolution was introduced through the analysis of Schallamach waves in terms of the stress-strain cycles at the leading edge of the interface. This insight leads to interesting predictions that will impact material design for the wide range of applications where Schallamach waves are observed or anticipated.

7.1.2 The Effect of a Single Defect on Soft Elastomeric Friction

A single defect or cut was used in two testing geometries, an elastomeric lens and an elastomeric flat surface, to model the sliding over a single feature's edge. The defects provided dramatic changes in the sliding frictional force when the defect was in the rear portion of the sliding contact area or in close proximity to the trailing edge. In the front portion of the contact area or ahead of the slider in the direction of travel, defects did not alter the sliding frictional force compared to a defect free surface. The drop associated with the defect could not be explained from changes in sliding contact area. Contact splitting and two correction factors are required to quantitatively describe the frictional impact of the defect. The most significant correction factor describes stiffness changes associated with the lateral proximity to the defect. The form of this correction factor was fit empirically to data on the shear resistance of a spherical slider on a flat elastomer

substrate. The other correction factor accounts for finite size effects associated with lateral confinement; previously established for normal contact experiments. Accounting for contact splitting and including the associated corrections factors, we accurately described the deviation of the data from the direct relationship of changes in force to changes in contact area.

7.1.3 The Friction of Aligned Surface Wrinkles

Using surfaces with aligned wrinkles of various aspect ratios, we have shown that surface wrinkles can drastically reduce the sliding frictional force of a hemispherical lens. The change in frictional force can not be described solely from changes in contact area, indicating that the wrinkles are not acting as "roughness" on the surface. Scaling was developed that describes the changes in sliding shear stress associated with the addition of wrinkles to a soft elastomeric surface. It was shown that three separate coefficients of friction are required to describe sliding parallel, perpendicular, and on a flat surface, even though these surfaces are comprised of identical materials, the only changes being the addition of topography. This work helps exemplify that the coefficient of friction is not a material property and is subjective to testing geometry.

7.1.4 The Alignment of Wrinkles through Surface Defects

A new technique was developed to align osmotically driven surface wrinkles sans lithographically defined topography or selective oxidation. This technique involves the addition of surface defects or cracks in a rigid film deposited on a soft elastomeric substrate. The cracks change the global biaxial stress state to a local uniaxial stress state. The aspect ratio of these features can be controlled by the film thickness, modulus of the elastomeric substrate, and the swelling agent used. The defects do not appear to alter the

aspect ratio of the wrinkles. The tuning of the aspect ration and the wrinkle alignment offer the ability to fully manipulate the friction and the sliding interface and even control the anisotropy.

7.2 Future Work

- It was noticed in the work on the friction of wrinkled surfaces that Schallamach waves could be disrupted sliding perpendicular to the wrinkles. It would be interesting to evaluate the critical aspect ratio required for this disruption of Schallamach waves and also compare it to the shape of Schallamach waves created on a flat surface.

- In most of the sliding experiments a single geometry was used: a fused silica hemispherical lens with a radius of curvature of 5 mm. From the experimental results presented here it is obvious that contact geometry plays a significant role in determining the sliding friction of an interface. Work should be conducted evaluating various probe geometries, further exploring all of the frictional topics discussed here.

- It would be interesting to evaluate the friction of chemically patterned surfaces aligned similar to the wrinkles presented in Chapter 4. In this case, no topography would be added to the surfaces and the interactions between the slider and surfaces would be altered with strips of chemical functionality. With a large enough difference in the adhesion between the slider and the respective functionalities, varying the widths of the respective functionalities should allow

for tuning of the frictional force. It would be interesting to see if these chemical patterns followed a similar inverse periodicity dependency on the sliding shear stress similar to topographic features.

- Wrinkled surfaces, which are not molded in the manner we used, naturally have residual stresses that develop upon wrinkling. We intentionally molded to remove these stresses and keep a uniform moduli and surface chemistry. It would be interesting to evaluate the friction of surface with residual stresses to see how the sliding friction changes. The SiO_x upper layer does not offer the chance to perform these experiments as it fractures upon sliding, giving yet another variable to take into account.

APPENDIX A

FRICTIONAL EXPERIMENTS

A.1 Assembly of the Apparatus

A more detailed explanation of the frictional testing will be given here. A simple schematic of the apparatus is shown in figure 3.1. A few details are omitted from the diagram but will be discussed here in full. The lever is attached to a custom made platform by clamping the bearing on either side. The bearings slide into pinch points, which lock the bearing in place but do not affect their rotation, through the use of screws. The bearing should be positioned using the shims made so that only the edge of the bearings are clamped and that the rotating portion is not restricted. The assembled bracket and lever are then mounted on an x stage which is attached to a y translating stage. It should be checked that the lever arm makes a 90 degree angle with the edge of the translating stage before it is attached to the x/y stage. The x and y stages are mounted on a z positioning stage which is mounted to a post on the breadboard with the microscope. The cable attached to the load cell should be attached to the breadboard with a consistent amount of excess slack in the cable. The cable should not be tight; it should droop at a fixed length below the load cell to control the force it applies to the cantilever. This is done by wrapping the cable around a screw which is tightened to the breadboard. Red tape should be wrapped around the end of the lever where the lens will be mounted. The lens should then be glued to the red tape using super glue. On the other end the appropriate number of washers and nut should be attached to achieve the desired normal loads. Also on the side with the counterweights, a nanopositioner with a load cell should be mounted in a vertical direction. This is to control the rate of interfacial formation. For

all tests completed in this work the lens was brought into contact with the substrate at a velocity of 10μm/s. An alternate function of the nanopositioner and load cell (mounted vertically) is to measure the exact load applied to the lens. When the lens is lifted off of the substrate the reading on the load cell and the distances to the pivot and the distance from the pivot to the lens can be used to calculate the applied normal load using the lever rule.

There are a few regular maintenance steps that should be completed to ensure the results are accurate and consistent. To confirm the setups accuracy of applied normal load bring it into contact with a substrate to ensure the contact area is consistent through multiple loadings. Also the load cell should be calibrated to ensure the volt to gram conversion in the LabVIEW program is accurate.

A.2 Running a Test

The power supply for the load cell needs to be turned on 15 minutes before testing to begin to warm up. Check to make sure the lever is flat when in contact with the substrate, the z positioner can be adjusted to fix this. Make sure the scope is turned on, the camera is plugged in, and the side port is selected on the scope. LabVIEW programs have been developed to automate the test. Enter the desired distance, velocity, and time between pictures when applicable. The actual velocity is not the imputed velocity and the following table (A.1) summarizes the differences.

In the live preview bring the lens into contact with the substrate. The lens has to be brought manually into contact with the substrate using the nanopositioner and the load should be noted. Use the x-y stages to center the lens in the image. Move the lens out of contact with the substrate then bring it back into contact at a fixed velocity. Allow one

minute of interfacial history before beginning the test. After each test completely raise the lens out of contact with the substrate, then pick up the lens and clean it with ethanol and lens paper between each test. Do not use Kimwipes as they will scratch glass.

Following an experiment the data will output time and force in grams. Some of the experiments will also output distance, if not it can be calculated by multiplying time by the actually output velocity. Lateral force in mN is calculated by multiplying the force in grams by 9.81.

Table A.1: Programmed velocity compared to actual output velocity.

Programmed Velocity (μm/s)	Actual Velocity(μm/s)
0.25	0.35
0.5	0.77
0.75	1.26
1	1.89
1.5	3.79
2	4.63
2.5	10.41
2.75	20.84
3	41.67
5	83.34

APPENDIX B

THE FRICTIONAL RESPONSE OF A RIGID FILM ON A SOFT ELASTOMERIC SUBSTRATE

B.1 Introduction

The sliding of a rigid lens on a rigid film deposited on an elastomeric substrate provides some interesting results from the brief set of experiments that were conducted on this topic. Experiments were conducted on a SiO_x layer deposited on PDMS through a UVO process similar to the processes in Chapters 5 and 6. This work allowed for the visualization of wrinkles ahead of the slider in the direction of travel that were similar to the surface wrinkles in Chapter 6. Wrinkling has been shown to be a useful metrology tool and could be used in this type of material system to calculate film thickness or modulus if the other were known. The other noticeable trait of sliding along a composite surface like the one mentioned here is fracture at the trailing edge. The frictional force could be used to calculate the fracture toughness of a film if some calibrations were run on model systems. Utilizing the wrinkling and the fracture, this could be used for a quick method to determine film thickness or modulus and fracture toughness. Figure B.1 shows both the fracture and wrinkling associated with this material system. Also noted in this figure are Schallamach waves. The wrinkles that occur ahead of the slider in the direction of travel are completely reversible, but the fractures lines at the trailing edge are permanent.

B.2 Experimental

PDMS samples were created using a crosslinker to prepolymer ratio of 1 to 10. One millimeter thick samples were cured at 70° for two hours. The samples were then exposed to ultraviolet light in the presence of ozone (UVO). The UVO exposure time was

0, 3, 6, 9, 12, 15, and 18 minutes. Samples were subjected to frictional experiments and contact adhesion test. Frictional experiments were conducted using the apparatus described in Chapter 3. The slider was a fused silica hemispherical lens with a radius of curvature of 5mm. The testing velocity was fixed at 5μm/s. The contact adhesion tests were conducted at 1μm/s and the maximum compressive force was fixed at 20 mN.

Similar to the frictional experiments a fused silica hemispherical lens with a radius of curvature of 5mm was used as the probe.

B.3 Results and Discussion

The average lateral force for all of the experiments was calculated and is shown in figure B.2.

The lateral force increased dramatically at low UVO exposure times. This is caused by the hydrophobic PDMS surface being converted a hydrophilic SiO_x surface which is more similar to the slider. The force then drops as the material becomes less conforming to the lens and the SiO_x layer increases in thickness. Also as the UVO time increases, fractures begin to occur at the trailing edge of the slider. These defects are identical to the single features described in Chapter 4, providing a decrease in the tangential stiffness of the sliding interface. These cracks were characterized and the results are shown in figure B.3.

In Figure B.3, a critical conversion of the upper surface to SiO_x must be achieved in order to fracture the surface while sliding. Initially the fracture spacing is large since the conversion is inhomogeneous. The sample with 9 minutes of UVO exposure has a thick enough SiO_x layer to fracture on a regular basis. As the exposure time increase the

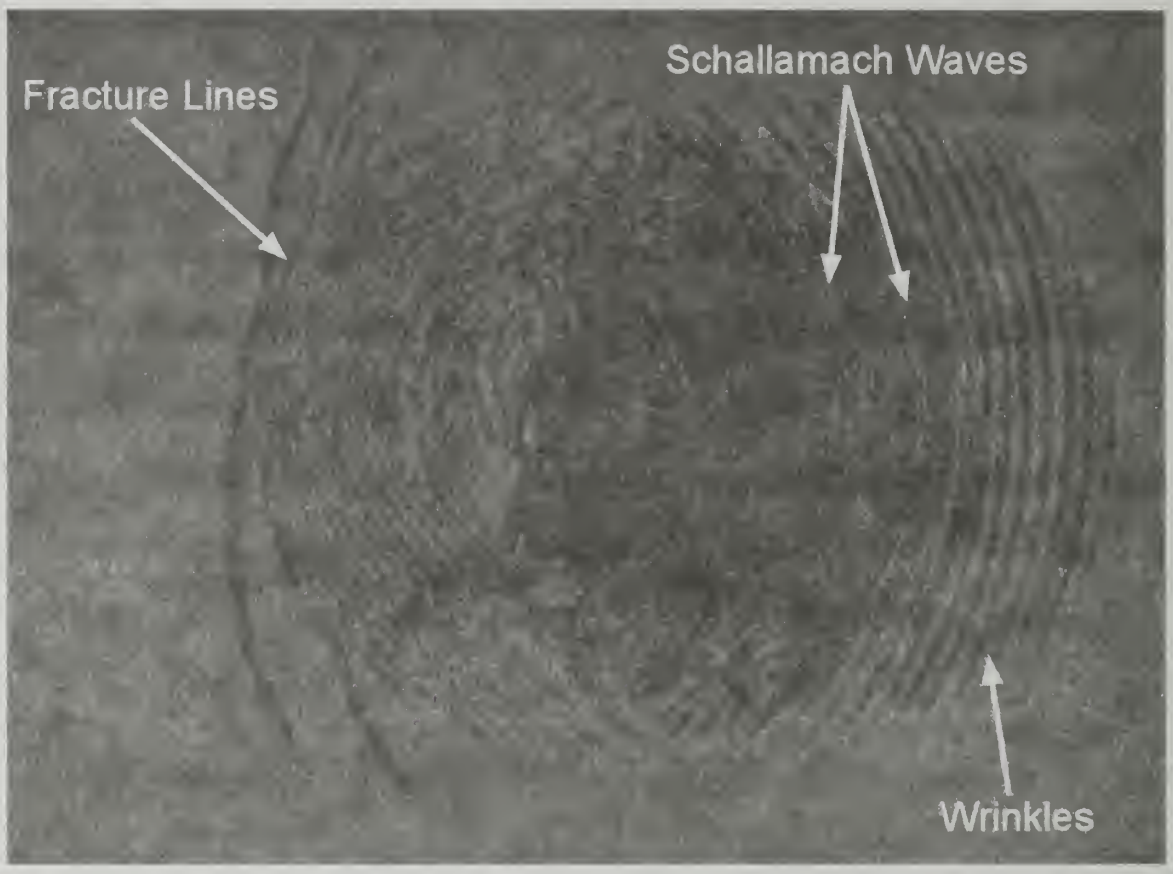

Figure B.1: Lens sliding on a rigid film mounted on a soft elastomeric substrate.

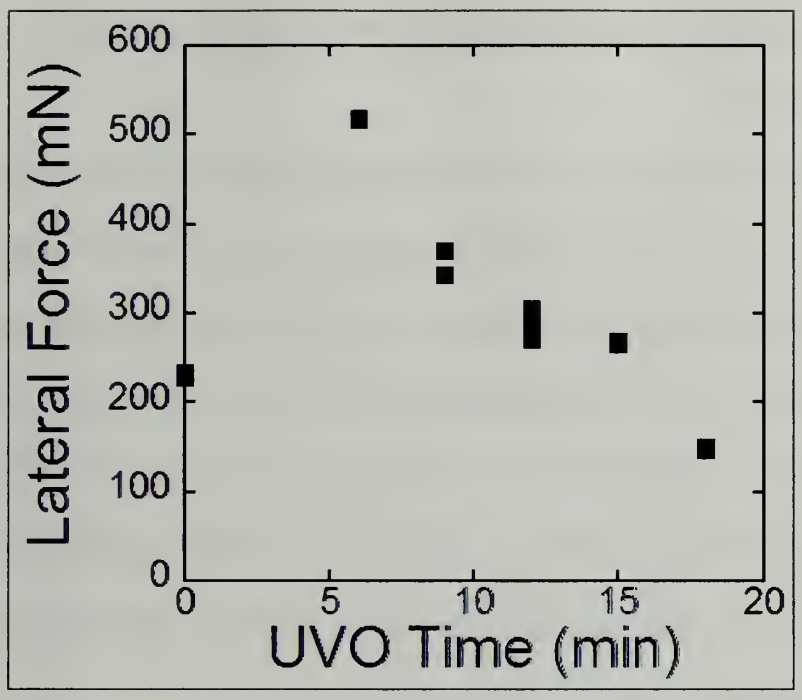

Figure B.2: Lateral force versus UVO exposure time.

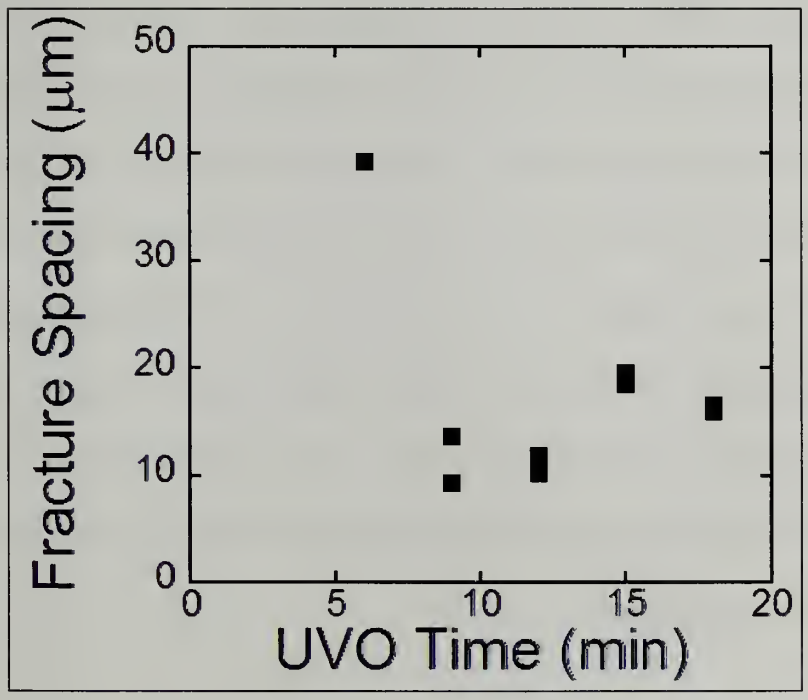

Figure B.3: Fracture spacing versus UVO exposure time.

thickness of the SiO_x layer increases and so does the fracture toughness of the SiO_x layer as seen in figure B.3.

The results of the contact adhesion tests are shown in figures B.4 and B.5. The conversion of the upper layer increase the stiffness of the surface as noted in figure B.4 where the modulus increases at the surface. As expected from the friction experiments the interfacial adhesion increases immediately upon conversion of the upper surface to a SiO_x layer as the surface chemistry becomes similar to the silica probe. The adhesion drops off as the SiO_x layer becomes more rigid and losses its ability to dissipate energy into the PDMS substrate. One thing to note is that the SiO_x layer never fractured during any of the contact adhesion tests.

B.4 Summary

It was shown that depositing a thin film on a soft surface provided some interesting results and has the potential of being used as a one step metrology device to measure film thickness or modulus and fracture toughness. Further experiments should be conducted on a model system where the thin film is applied to the surface and not a diffusion controlled conversion of the surface. Using our material system we confirmed that the UVO process changed the surface chemistry of PDMS substrate as noted in contact adhesion tests. These tests also showed that the conversion and thickness of the SiO_x layer increased with exposure time as was noted in modulus measurements. Fractures were noticed during frictional experiments, but they were never noticed in contact adhesion experiments.

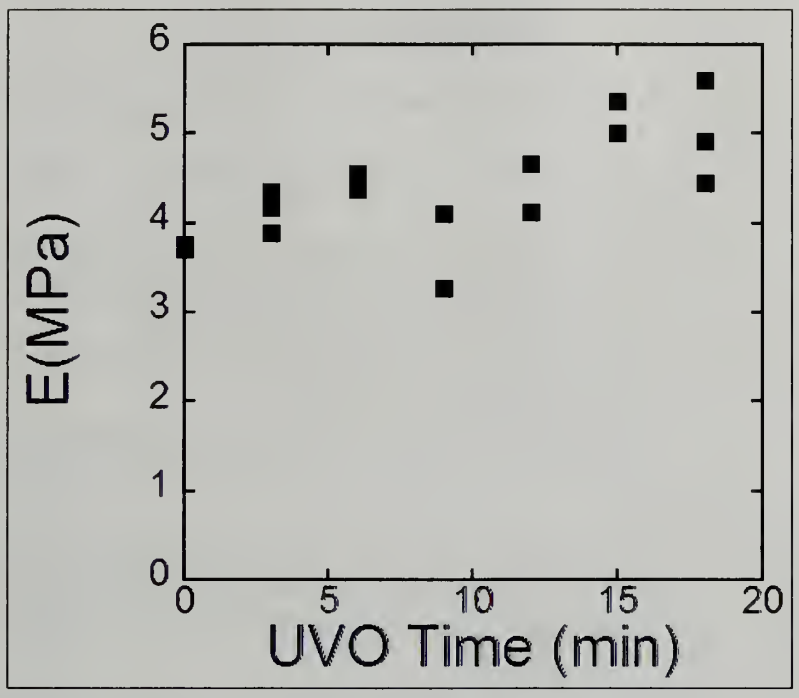

Figure B.4: Measured modulus at the surface versus UVO exposure.

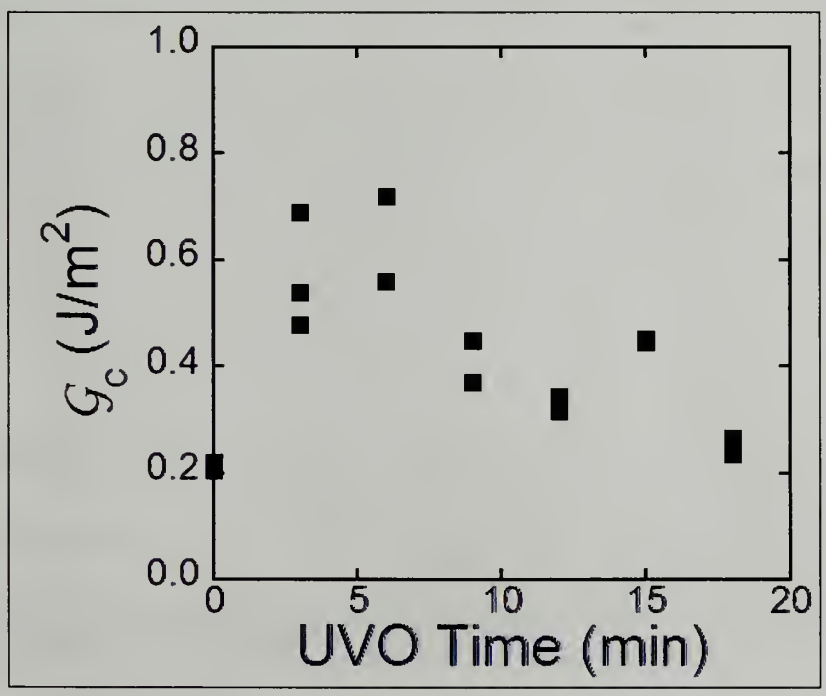

Figure B.5: Critical energy release rate (G_c) versus UVO exposure time.

BIBLIOGRAPHY

1. Bowden, F.P.T., D., *The Friction and Lubrication of Solids*. 1964, Oxford: Clarendon Press.
2. Autumn, K., et al., *Adhesive force of a single gecko foot-hair.* Nature, 2000. **405**(6787): p. 681-685.
3. Arzt, E., S. Gorb, and R. Spolenak, *From micro to nano contacts in biological attachment devices.* Proceedings Of The National Academy Of Sciences Of The United States Of America, 2003. **100**(19): p. 10603-10606.
4. Persson, B.N.J., *On the mechanism of adhesion in biological systems.* Journal Of Chemical Physics, 2003. **118**(16): p. 7614-7621.
5. Greiner, C., A. del Campo, and E. Arzt, *Adhesion of bioinspired micropatterned surfaces: Effects of pillar radius, aspect ratio, and preload.* Langmuir, 2007. **23**(7): p. 3495-3502.
6. Aksak, B., M.P. Murphy, and M. Sitti, *Adhesion of biologically inspired vertical and angled polymer microfiber arrays.* Langmuir, 2007. **23**(6): p. 3322-3332.
7. Geim, A.K., et al., *Microfabricated adhesive mimicking gecko foot-hair.* Nature Materials, 2003. **2**(7): p. 461-463.
8. Glassmaker, N.J., et al., *Biologically inspired crack trapping for enhanced adhesion.* Proceedings Of The National Academy Of Sciences Of The United States Of America, 2007. **104**(26): p. 10786-10791.
9. Crosby, A.J., M. Hageman, and A. Duncan, *Controlling polymer adhesion with "pancakes".* Langmuir, 2005. **21**(25): p. 11738-11743.
10. Hui, C.Y., et al., *Design of biomimetic fibrillar interfaces: 2. Mechanics of enhanced adhesion.* Journal Of The Royal Society Interface, 2004. **1**(1): p. 35-48.
11. Glassmaker, N.J., et al., *Design of biomimetic fibrillar interfaces: 1. Making contact.* Journal Of The Royal Society Interface, 2004. **1**(1): p. 23-33.
12. Schallamach, A., *How Does Rubber Slide?* Wear, 1971. **17**(4): p. 301-312.
13. Johnson, K.L., K. Kendall, and A.D. Roberts, *Surface Energy And Contact Of Elastic Solids.* Proceedings Of The Royal Society Of London Series A-Mathematical And Physical Sciences, 1971. **324**(1558): p. 301-313.
14. Green, A.E. and W. Zerna, *Theoretical Elasticity*. 1954, Oxford.
15. Biot, M.A., *Surface Instability In Finite Anisotropic Elasticity Under Initial Stress.* Proceedings Of The Royal Society Of London Series A-Mathematical And Physical Sciences, 1963. **273**(135): p. 329-339.
16. Tanaka, T., et al., *Mechanical Instability Of Gels At The Phase-Transition.* Nature, 1987. **325**(6107): p. 796-798.
17. Bowden, N., et al., *Spontaneous formation of ordered structures in thin films of metals supported on an elastomeric polymer.* Nature, 1998. **393**(6681): p. 146-149.
18. Chan, E.P. and A.J. Crosby, *Spontaneous formation of stable aligned wrinkling patterns.* Soft Matter, 2006. **2**(4): p. 324-328.
19. Chan, E.P. and A.J. Crosby, *Fabricating microlens arrays by surface wrinkling.* Advanced Materials, 2006. **18**(24): p. 3238-+.
20. Chan, E.P., et al., *Surface Wrikles for Smart Adhesion.* Advanced Materials-Accepted, 2007.

21. Chen, X. and J.W. Hutchinson, *A family of herringbone patterns in thin films.* Scripta Materialia, 2004. **50**(6): p. 797-801.
22. Efimenko, K., et al., *Nested self-similar wrinkling patterns in skins.* Nature Materials, 2005. **4**(4): p. 293-297.
23. Harrison, C., et al., *Sinusoidal phase grating created by a tunably buckled surface.* Applied Physics Letters, 2004. **85**(18): p. 4016-4018.
24. Stafford, C.M., et al., *A buckling-based metrology for measuring the elastic moduli of polymeric thin films.* Nature Materials, 2004. **3**(8): p. 545-550.
25. Southern, E. and A.G. Thomas, *Effect Of Constraints On Equilibrium Swelling Of Rubber Vulcanizates.* Journal Of Polymer Science Part A-General Papers, 1965. **3**(2PA): p. 641-646.
26. Barquins, M. and R. Courtel, *Rubber Friction And Rheology Of Viscoelastic Contact.* Wear, 1975. **32**(2): p. 133-150.
27. Barquins, M., *Adherence, Friction And Wear Of Rubber-Like Materials.* Wear, 1992. **158**(1-2): p. 87-117.
28. Koudine, A.A. and M. Barquins, *On the influence of rubber thickness on the existence of Schallamach waves.* International Journal Of Adhesion And Adhesives, 1997. **17**(2): p. 107-110.
29. Barquins, M. and A.D. Roberts, *Rubber-Friction Variation With Rate And Temperature - Some New Observations.* Journal Of Physics D-Applied Physics, 1986. **19**(4): p. 547-563.
30. Rand, C.J. and A.J. Crosby, *Insight into the periodicity of Schallamach waves in soft material friction.* Applied Physics Letters, 2006. **89**(26).
31. Shull, K.R., *Contact mechanics and the adhesion of soft solids.* Materials Science & Engineering R-Reports, 2002. **36**(1): p. 1-45.
32. Chaudhury, M.K., *Rate-dependent fracture at adhesive interface.* Journal Of Physical Chemistry B, 1999. **103**(31): p. 6562-6566.
33. Perutz, S., et al., *Investigation of adhesion hysteresis in poly(dimethylsiloxane) networks using the JKR technique.* Journal Of Polymer Science Part B-Polymer Physics, 1998. **36**(12): p. 2129-2139.
34. Russell, A.P., *Contribution To Functional-Analysis Of Foot Of Tokay, Gekko-Gecko (Reptilia-Gekkonidae).* Journal Of Zoology, 1975. **176**(AUG): p. 437-476.
35. Autumn, K. and A.M. Peattie, *Mechanisms of adhesion in geckos.* Integrative And Comparative Biology, 2002. **42**(6): p. 1081-1090.
36. Ge, L., et al., *Carbon nanotube-based synthetic gecko tapes.* Proceedings Of The National Academy Of Sciences Of The United States Of America, 2007. **104**(26): p. 10792-10795.
37. Sitti, M. and R.S. Fearing, *Synthetic gecko foot-hair micro/nano-structures as dry adhesives.* Journal Of Adhesion Science And Technology, 2003. **17**(8): p. 1055-1073.
38. Gorb, S., et al., *Biomimetic mushroom-shaped fibrillar adhesive microstructure.* Journal Of The Royal Society Interface, 2007. **4**(13): p. 271-275.
39. Ge, L., et al., *Carbon nanotube-based synthetic gecko tapes.* Proc Natl Acad Sci U S A, 2007. **104**(26): p. 10792-5.
40. Majidi, C., et al., *High friction from a stiff polymer using microfiber arrays.* Physical Review Letters, 2006. **97**(7).

41. Niederegger, S. and S.N. Gorb, *Friction and adhesion in the tarsal and metatarsal scopulae of spiders.* J Comp Physiol A Neuroethol Sens Neural Behav Physiol, 2006. **192**(11): p. 1223-32.
42. Rand, C.J. and A.J. Crosby, *Friction of soft elastomeric surfaces with a defect.* Applied Physics Letters, 2007. **91**(26).
43. Johnson, K.L., *Contact Mechanics*. 9th ed. 2003, Cambridge, UK: Cambridge University Press.
44. Carpick, R.W., et al., *Atomic-scale friction and its connection to fracture mechanics.* Jom, 2004. **56**(10): p. 48-52.
45. Shull, K.R., et al., *Axisymmetric adhesion tests of soft materials.* Macromolecular Chemistry And Physics, 1998. **199**(4): p. 489-511.
46. Shull, K.R. and A.J. Crosby, *Axisymmetric adhesion tests of pressure sensitive adhesives.* Journal Of Engineering Materials And Technology-Transactions Of The Asme, 1997. **119**(3): p. 211-215.
47. Chung, J.Y. and M.K. Chaudhury, *Roles of discontinuities in bio-inspired adhesive pads.* Journal Of The Royal Society Interface, 2005. **2**(2): p. 55-61.
48. Kim, S. and M. Sitti, *Biologically inspired polymer microfibers with spatulate tips as repeatable fibrillar adhesives.* Applied Physics Letters, 2006. **89**(26).
49. Matsuo, E.S. and T. Tanaka, *Patterns In Shrinking Gels.* Nature, 1992. **358**(6386): p. 482-485.
50. Chan, E.P., et al., *Surface wrinkles for smart adhesion.* Advanced Materials, 2008. **20**(4): p. 711-+.
51. Heuberger, M., G. Luengo, and J.N. Israelachvili, *Tribology of shearing polymer surfaces. 1. Mica sliding on polymer (PnBMA).* Journal Of Physical Chemistry B, 1999. **103**(46): p. 10127-10135.
52. Carbone, G. and L. Mangialardi, *Adhesion and friction of an elastic half-space in contact with a slightly wavy rigid surface.* Journal Of The Mechanics And Physics Of Solids, 2004. **52**(6): p. 1267-1287.
53. Guduru, P.R., *Detachment of a rigid solid from an elastic wavy surface: Theory.* Journal Of The Mechanics And Physics Of Solids, 2007. **55**(3): p. 445-472.
54. Johnson, K.L., *The Adhesion Of 2 Elastic Bodies With Slightly Wavy Surfaces.* International Journal Of Solids And Structures, 1995. **32**(3-4): p. 423-430.
55. Hui, C.Y., et al., *The mechanics of contact and adhesion of periodically rough surfaces.* Journal Of Polymer Science Part B-Polymer Physics, 2001. **39**(11): p. 1195-1214.
56. Ouyang, M., et al., *Conversion of some siloxane polymers to silicon oxide by UV/ozone photochemical processes.* Chemistry Of Materials, 2000. **12**(6): p. 1591-1596.
57. Barquins, M., *Sliding Friction Of Rubber And Schallamach Waves - A Review.* Materials Science And Engineering, 1985. **73**(1-2): p. 45-63.
58. Johnson, K.L., J.A. Greenwood, and J.G. Higginson, *The Contact Of Elastic Regular Wavy Surfaces.* International Journal Of Mechanical Sciences, 1985. **27**(6): p. 383-&.
59. Cerda, E. and L. Mahadevan, *Geometry and physics of wrinkling.* Physical Review Letters, 2003. **90**(7).

60. Kaelble, D.H., *Theory And Analysis Of Peel Adhesion - Mechanisms And Mechanics.* Transactions Of The Society Of Rheology, 1959. **3**: p. 161-180.
61. Koudine, A.A. and M. Barquins, *Formation of micro-ridges on the surface of Schallamach waves propagating in the contact area between a moving rubber sample and a glass lens.* Journal Of Adhesion Science And Technology, 1996. **10**(10): p. 951-961.
62. Chua, D.B.H., H.T. Ng, and S.F.Y. Li, *Spontaneous formation of complex and ordered structures on oxygen-plasma-treated elastomeric polydimethylsiloxane.* Applied Physics Letters, 2000. **76**(6): p. 721-723.
63. Bowden, N., et al., *The controlled formation of ordered, sinusoidal structures by plasma oxidation of an elastomeric polymer.* Applied Physics Letters, 1999. **75**(17): p. 2557-2559.
64. Mirley, C.L. and J.T. Koberstein, *A Room-Temperature Method For The Preparation Of Ultrathin Siox Films From Langmuir-Blodgett Layers.* Langmuir, 1995. **11**(4): p. 1049-1052.
65. Efimenko, K., W.E. Wallace, and J. Genzer, *Surface modification of Sylgard-184 poly(dimethyl siloxane) networks by ultraviolet and ultraviolet/ozone treatment.* Journal Of Colloid And Interface Science, 2002. **254**(2): p. 306-315.
66. Allen, H.G., *Analysis and Design of Structural Sandwich Panels.* 1969, Oxford: Pergamon Press.
67. Rand, C.J., et al., *Fracture Induced Alignment of Surface Wrinkles.* Soft Matter, 2008.
68. Heinrich, M., et al., *Dimensional control of brittle nanoplatelets. A statistical analysis of a thin film cracking approach.* Nano Letters, 2006. **6**(9): p. 2026-2030.
69. Chiang, M.Y.M.W., W.; He, J.; Amis, E. J., *Combinatorial approach to the edge delamination test for thin film reliability—concept and simulation.* Thin Solid Films, 2003. **437**: p. 197-203.
70. Chan, E.P., et al., *Surface Wrinkles for Smart Adhesion.* Advanced Materials, 2008: p. NA.
71. Duffy, D.C., et al., *Rapid prototyping of microfluidic systems in poly(dimethylsiloxane).* Analytical Chemistry, 1998. **70**(23): p. 4974-4984.
72. Ned, B., et al., *The controlled formation of ordered, sinusoidal structures by plasma oxidation of an elastomeric polymer.* Applied Physics Letters, 1999. **75**(17): p. 2557-2559.